arXiv:1610.09781v1 [astro-ph.GA] 31 Oct 2016

On the Newtonian and spin-induced perturbations felt by the stars orbiting around the massive black hole in the Galactic Center

Fupeng Zhang[1,†] and Lorenzo Iorio[2]

[1] *School of Physics and Astronomy, Sun Yat-Sen University, Guangzhou 510275, China;* † *zhangfp7@mail.sysu.edu.cn*

[2] *Ministero dell' Istruzione, dell' Università e della Ricerca (M.I.U.R.)-Istruzione, Fellow of the Royal Astronomical Society (F.R.A.S.) Viale Unità di Italia 68, 70125, Bari (BA), Italy; lorenzo.iorio@libero.it*

ABSTRACT

The S-stars discovered in the Galactic center (GC) are expected to provide unique dynamical tests of the Kerr metric of the massive black hole (MBH) orbited by them. In order to obtain unbiased measurements of its spin and the related relativistic effects, a comprehensive understanding of the gravitational perturbations of the stars and stellar remnants around the MBH is quite essential. Here, we study the perturbations on the observables of a typical target star, i.e., the apparent orbital motion and the redshift, due to both the spin-induced relativistic effects and the Newtonian attractions of a single or a cluster of disturbing object(s). We find that, in most cases, the Newtonian perturbations on the observables are mainly attributed to the perturbed orbital period of the target star, rather than the Newtonian orbital precessions. The Newtonian perturbations have their unique features when they peak around the pericenter passage in each revolution, which is quite different from those of the spin-induced effects. Looking at the currently detected star S2/S0-2, we find that its spin-induced effects on both the image position and redshift are very likely obscured by the gravitational perturbations from the star S0-102 alone. We also investigate and discuss the Newtonian perturbations on a hypothetical S-star located inside the orbits of the currently detected ones. By considering a number of possible stellar distributions near the central MBH, we find that the spin-induced effects on the apparent position and the redshift dominate over the stellar perturbations for target stars with orbital semimajor axis smaller than $100 - 400$ AU if the MBH is maximally spinning. Our results suggest that, in principle, the stellar perturbations can be removed as they have distinctive morphologies comparing to those of the relativistic Kerr-type signatures.

Subject headings: black hole physics – Galaxy: center – Galaxy: nucleus – gravitation – relativistic processes – stars: kinematics and dynamics

1. Introduction

It is now widely accepted that a massive black hole (MBH) exists in the center of our galaxy, with the most prominent evidence provided by the so-far Keplerian motion of dozens of the surrounding S-stars (Ghez et al. 2008; Gillessen et al. 2009). They are found to be exclusively B-type dwarfs, and closely orbiting the central MBH within a distance of $\sim$ 0.04pc$\simeq$ 8250 AU. The continuous monitoring of their orbital motion provides precise measurements of the mass of the central MBH ($\simeq 4 \times 10^6 M_\odot$) and, simultaneously, of the Galactic distance ($\simeq 8\,$kpc) (Ghez et al. 2008; Gillessen et al. 2009; Meyer et al. 2012). Theoretical studies suggest that some of the hidden S-stars exist within the orbits of the currently detected ones, which may be revealed by the future telescopes, e.g., the thirty meter telescope (TMT) or European extremely large telescope (E-ELT) (e.g., Zhang et al. 2013). Due to the proximity of these S-stars to the MBH, the strength of the gravitational field around them is orders of magnitude larger than those in the solar system and the pulsar binaries (Angélil et al. 2010; Iorio 2011a). Thus, their trajectories contain various general relativistic (GR) effects, including the Lense-Thirring precession and the frame dragging (e.g., Jaroszynski 1998; Fragile & Mathews 2000; Rubilar & Eckart 2001; Weinberg et al. 2005; Will 2008; Preto & Saha 2009; Angélil et al. 2010; Angélil & Saha 2010, 2011; Merritt et al. 2010; Iorio 2011a,b; Zhang et al. 2015), which should be measured accurately by the powerful facilities in the near future. The continuous tracking of the orbital motion of the S-stars by the future telescopes is expected to provide unique dynamical tests of the Kerr metric of the MBH and also the no-hair theorem in the Galactic center (GC) (e.g., Zhang et al. 2015; Psaltis et al. 2015; Johannsen 2016; Yu et al. 2016).

However, in order to make the accurate measurements of the spin and its induced GR effects actually feasible, a careful handling of the perturbations induced by the other stars on the motion of the target ones (The so-called "Newtonian perturbation" or the "stellar perturbation") is required. Indeed, they are likely contributed by a number of different gravitational sources located in the vicinity of the target star in the GC, e.g., the late-type and early-type stars (e.g., Paumard et al. 2006; Gillessen et al. 2009; Bartko et al. 2010), stellar mass black holes, neutron stars, white dwarfs (e.g., Freitag et al. 2006; Morris 1993), and dark matters (e.g., Iorio 2013). An intermediate mass black hole (IMBH) possibly exists, with some allowed parameter space for its orbit and mass according to the current observations (e.g., Hansen & Milosavljević 2003; Yu & Tremaine 2003; Genzel et al. 2010; Gualandris & Merritt 2009; Gillessen et al. 2009; Gualandris et al. 2010). Other dynamical processes, e.g., gravitational wave and tidal dissipation, are important but only for those S-stars in highly eccentric orbits and/or in extremely tight orbits (Psaltis 2012; Psaltis et al. 2013, 2015).

The stellar perturbation can induce additional orbital precessions of the target star and submerge those due to the spin-induced effects. N-body post-Newtonian numerical simulations (Merritt et al. 2010) or the analytical estimations base on the orbital perturbing theories (Sadeghian & Will 2011), both found that the orbital precessions of the target star caused by the stellar perturbations can obscure those due to the frame-dragging effects (or the quadrupole effects) if the target star itself is located outside distance of $\sim$ 0.5mpc (or $\sim$ 0.2mpc) from the MBH. However, these previous

studies have not included other complexities. For example, the precessions of the ascending node, periapsis and the orbital inclination can only be indirectly determined by fitting the predictions of models incorporating the various GR effects and also the complexities due to the MBH parameters (e.g., mass, spin and GC distance) to the directly observables of the target star, i.e., the apparent trajectories in the plane of the sky and the redshift. Thus, from a practical point of view, it is more meaningful to compare the predicted perturbations on the apparent trajectories and redshifts of the target star due to spin effects to those due to the stellar perturbations.

In our previous study (Zhang et al. 2015, here after ZLY15), we have developed a fast full general relativistic method to obtain the observables of the target star by both considering its orbital motion around the MBH and the propagation of photons from the target star to a distance observer. We investigated the constraints of the spin parameters by fitting to the observables of the target star without considering the stellar perturbations. Relying upon the framework of ZLY15, here we further include the gravitational perturbations due to a single or a cluster of disturbing object(s) on the orbital motion of the target stars orbiting the MBH. By performing a large number of numerical simulations, we investigate the Newtonian perturbations on the apparent orbital motion and the redshift of the target star and their dependences on the model parameters. The differences between the spin-induced relativistic effects and the Newtonian perturbations revealed by our study can provide useful clues of their separation methods, which are quite essential for the accurate measurements of the spin parameters and also the tests of the Kerr metric.

This paper is organized as follows. Section 2 describes the details of the numerical methods. The gravitational attractions of the background perturbers are included as an additional perturbed Hamiltonian term in the equations of motion of the target star. To obtain the projected sky position and the redshift of the star at a given moment, we adopt the light tracing technique described in ZLY15 to solve the light trajectories propagating from the star to the observer. In Section 3, we describe the details of the methods used to estimate the perturbations on the apparent position and redshift of the target star due to the GR spin effects, Newtonian perturbations and their combined effects from the numerical simulations. In Section 4, we investigate the stellar perturbations caused by a single perturber, in the specific case that S2/S0-2 is perturbed by the gravitational force of S0-102 (Section 4.1), or in the general case that a hypothetical S-star located inside the orbits of the current detected ones is perturbed by a single perturber (Section 4.2). In Section 5, we consider the stellar perturbations of a cluster of disturbing objects. By performing a large number of numerical simulations, we investigate their resulting perturbations on the observables and comparing them to those of the spin-induced signals. The discussions and conclusions are provided in Section 6 and Section 7, respectively.

2. Perturbed motion of the target star

The geodesic motion of a star orbiting a Kerr black hole (Kerr 1963) can be described by a Hamiltonian $H_{\rm K}$. In the Boyer-Lindquist coordinates (r, θ, ϕ, t) (Boyer & Lindquist 1967), it is

given by

$$H_{\rm K} = -\frac{(r^2+a^2)^2 - a^2\Delta\sin^2\theta}{2\Sigma\Delta}p_t^2 - \frac{2ar}{\Sigma\Delta}p_t p_\phi + \frac{\Delta}{2\Sigma}p_r^2 + \frac{1}{2\Sigma}p_\theta^2 + \frac{\Delta - a^2\sin^2\theta}{2\Sigma\Delta\sin^2\theta}p_\phi^2 \tag{1}$$

where

$$\begin{cases} \Sigma &= r^2 + a^2\cos^2\theta, \\ \Delta &= r^2 - 2r + a^2. \end{cases} \tag{2}$$

Here p_t, p_r, p_θ and p_ϕ are the components of the tetrad-momentum in the Boyer-Lindquist coordinate. Moreover, $a = Jc/(M_\bullet^2 G)$ is the dimensionless spin parameter of the MBH, J is the spin angular momentum of the MBH. For simplicity, we set $G = c = M_\bullet = r_{\rm g} = GM_\bullet/c^2 = 1$ above, G, c, $M_\bullet$ and $r_{\rm g}$ are the gravitational constant, the speed of light, the MBH mass, and the gravitational radius, respectively. Throughout this paper, we assume that the MBH in the GC is with a mass of $M_\bullet = 4\times10^6 M_\odot$ and a distance of $R_{\rm GC} = 8$ kpc. The corresponding gravitational radius is then given by $r_{\rm g} \simeq 0.04$ AU $\simeq 5\mu$as$\simeq 2\times10^{-4}$ mpc.

The equations of motion described by $H = H_{\rm K}$ can be further reduced to Equation 19-22 in ZLY15, from which we integrate numerically the orbital trajectories of a star without any stellar perturbation. As the Hamiltonian relies upon the full Kerr metric, all the various GR effects in the orbital motion of the target star around the Kerr MBH, including the advancements in the periastron and the orbital plane caused by the spin-induced effects, e.g., the frame dragging and the quadrupole effects, are thus simultaneously included in the simulations.

If the target star is surrounded by $N_{\rm p}$ perturbers, for example, a cluster of stars or stellar remnants in the field, the gravitational attractions from these sources can deviate the orbital motion of the target star from the GR prediction. Considering only the leading order perturbations in Newtonian gravity, we ignore the mutual gravitational interactions between the perturbers and take the target star as a test particle[1], then the perturbations on the target star contributed by these sources can be approximately expressed by a Hamiltonian $H_{\rm p}$, which is given by (see also Angélil & Saha 2014; Wisdom & Holman 1991),

$$H_{\rm p} = \sum_j^{N_{\rm p}} m_{{\rm p},j}\left(\frac{r}{r_j^2}\cos\zeta_j - \frac{1}{d}\right) \tag{3}$$

Here (r_j, θ_j, ϕ_j) and $m_{{\rm p},j}$ is the spatial position and the mass of the j-th perturber, respectively. $\zeta_j = \arccos\left[\sin\theta\sin\theta_j\cos(\phi-\phi_j) + \cos\theta\cos\theta_j\right]$ is the angle between the position vector of the target star and that of the j-th perturber, and $d = \sqrt{r^2 + r_j^2 - 2rr_j\cos\zeta_j}$ is the distance between

[1]We notice that assuming a non-zero mass of the target star could possibly lead to nonnegligible back-reaction effects on the motion of the MBH and the perturbers. We defer the exploration of such potentially relevant effects for future works.

the target star and the j-th perturber. Then the motion of the perturbed target star can be described by the modified Hamiltonian $H = H_{\rm K} + H_{\rm p}$. Note that as the mutual perturbations between the perturbers are disregarded, the orbital motion of each perturber rotating around the black hole can be fully described by Hamiltonian $H = H_{\rm K}$ and integrated by Equation 19-22 in ZLY15.

The orbital evolutions of the target star and the perturbers can be integrated from their Hamiltonian equations of motion once the initial orbital elements of the star and of the perturbers, and also the mass, the spin parameters and the distance of the MBH are provided (see details in ZLY15). Here the six orbital elements of the target star (the perturber) are the semimajor axis $a_\star$ ($a_{\rm p}$), eccentricity $e_\star$ ($e_{\rm p}$), inclination $I_\star$ ($I_{\rm p}$), longitude of position angle of the ascending node $\Omega_\star$ ($\Omega_{\rm p}$), arguments of angle to periapsis $\omega_\star$ ($\omega_{\rm p}$), and the true anomaly $f_\star$ ($f_{\rm p}$) [or the time of pericenter passage $t_{0\star}$ ($t_{0{\rm p}}$)], which are defined respective to the sky plane. The spin direction of the MBH is defined by two angles: i and ϵ. Here i is the line of sight inclination of the spin, ϵ is the angle between the projection of the direction of the spin onto the sky plane and a reference direction [2].

The observed sky position and the redshift of the target star can be obtained if the parameters describing the light trajectory emitted from the star to the distant observer are determined. As the spin-induced position difference of the star in the sky plane are found approximately the same order of magnitude compared to those caused by light-bending effects, it is crucial to include the light-tracing technique in the simulations to model accurately the apparent position of the star (See Section 5.1 in ZLY15). As the total enclosed mass of the perturbers distributed around the MBH (typically $\lesssim$ 10mpc in this paper, see also Section 5) are much smaller than the mass of the central MBH, we assume that the light trajectories can be approximately integrated by the equations of motion in the Kerr metrics. In this work, we adopt the backward light-tracing technique described in ZLY15 to calculate the observed right ascension (R.A.), the declination (Dec) of the target star in the sky plane, and also the redshift (Z) of the target star as a function of the observational time $t_{\rm obs}$ for an observer located at distance $R_{\rm GC}$. Here $t_{\rm obs} = t_\star + t_{\rm prop}$, $t_\star$ is the local time of the star in the Boyer-Lindquist coordinates and $t_{\rm prop}$ is the time used for a photon propagating from the star to the observer. All of the various GR effects affecting the propagations of the photons from the star to the observer, including both the displacement of the image position in the sky plane due to the gravitational light-bending and the gravitational redshift of the target star (e.g.,Iorio 2011b; Angélil et al. 2010; ZLY15), are then simultaneously included in the mock observables of the target star.

The full GR effects can be divided into two parts: the spin-zero and the spin-induced effects. The spin-zero effects are those when the black hole is not spinning, e.g., the Schwarzschild pre-

[2]For the definitions of the orbital elements of the star and the spin angles of the MBH please see the Figure 1 in ZLY15, identifying $a_\star = a'_{\rm orb}$, $e_\star = e'_{\rm orb}$, $I_\star = I'$, $\Omega_\star = \Omega'$, $\omega_\star = \Upsilon'$ and $f_\star = \nu'$ for $a'_{\rm orb}$, $e'_{\rm orb}$, I', Ω', Υ' and ν' defined in ZLY15.

cession, the time dilation, and etc. The spin-induced effects include the frame-dragging ($\propto a$), quadrupole momentum ($\propto a^2$), and other high order spin-related GR effects as well. Both of the spin-zero and the spin-induced effects have been automatically included in the orbital motion and the mock observables of the target star as we adopt a full Kerr metric. However, in the following sections, we deal only with the spin-induced effects, and single them out by removing the spin-zero effects from the full GR effects. For a given set of initial conditions, this can be done by examining the differences between the results of the simulation with $a = 0.99$ and that with $a = 0$ (See details in Section 3). We will not discuss about the effects of the spin-zero terms as they does not have direct connections to the purpose of this study. We defer the discussions of the spin-zero effects and their differences with the Newtonian perturbations to future works.

The Keplerian orbital elements of a star can be obtained by its instantaneous position and velocity. In this work, we calculate the orbital elements of the target star at any given moment by its three-position and three-velocity measured in the local non-rotating rest frame (LNRF) of the target star. Here the three-velocity can be derived according to Eq. 9-11 of ZLY15. We notice that if alternatively the elements are estimated by instantaneous position and the momentum in the LNRF frame (see also Preto & Saha 2009), the results will be slightly different. We also notice that the orbital elements calculated in this work can be different with those obtained in the post-Newtonian (PN) simulations, as the adopted spacetime metrics are different. However, we find that the results of these two methods are generally consistent (See more details in Section 4.1.3).

3. Evaluating the perturbations felt by the target star

The orbital motion and the observables of a target star rotating around a spinning black hole can be affected by both the spin-induced effects and the gravitational attractions from other stars/stellar remnants. In this work, we mainly deal with three types of perturbations experienced by the target star: (1) The spin-induced perturbation; (2) The Newtonian perturbation; (3) The combination of (1) and (2). If Y is any quantity relative to the motion of the target star, then the three types of perturbations listed above can be denoted as $\delta_{\rm s}Y$, $\delta_{\rm p}Y$ and $\delta_{\rm c}Y$, respectively. Here, Y can be any one of the orbital elements of the target star, e.g., $a_\star$, $e_\star$, $I_\star$, $\Omega_\star$, $\omega_\star$, $f_\star$, $\cdots$, or the observables, e.g., the coordinates of the apparent position (R.A. and Dec) and the redshift (Z) of the star. Note that Y can also be the position vector of the target star appeared in the sky plane, i.e., $\mathbf{R} =$ (R.A., Dec); then, its perturbations are denote as $\delta\mathbf{R} = (\delta\text{R.A.}, \delta\text{Dec})$.

The three types of the perturbations can be obtained by comparing between two simulations that have the same set of the initial orbital parameters of the target star and the perturber(s), however, the effects of spin and/or Newtonian gravities are turned on in one simulation and off in the other: (1) $\delta_{\rm s}Y$ is the difference of Y in the simulation with $a = 0$ and that with $a = 0.99$, both of which ignore the stellar perturbations; (2) $\delta_{\rm p}Y$ is the difference of Y in the simulation ignoring and that including the Newtonian gravities of the perturbers, both of which the spin is set to $a = 0$. (3) $\delta_{\rm c}Y$ is the difference of Y between the simulation including both the Newtonian

and spin-induced perturbations, and that ignoring both of them. We found that $\delta_{\rm c}Y \simeq \delta_{\rm p}Y + \delta_{\rm s}Y$.

As showed in the following sections, the signals of all these perturbations usually vary significantly as a function of time. The overall contributions of these perturbations can be estimated by their root mean squared values. Within a period of time $T_{\rm tot}$, the root mean squared (RMS) perturbation in Y is defined by

$$\overline{\delta Y} = \sqrt{\frac{1}{T_{\rm tot}} \int^{T_{\rm tot}} \delta Y(t_{\rm obs})^2 dt_{\rm obs}}. \tag{4}$$

Note that for the apparent position vector of the target star, i.e., $\mathbf{R}$ = (R.A., Dec), the RMS magnitude of its perturbation, i.e., $|\delta\mathbf{R}| = \sqrt{\delta{\rm Dec}^2 + \delta{\rm R.A.}^2}$, is defined by

$$\overline{|\delta\mathbf{R}|} = \sqrt{\frac{1}{T_{\rm tot}} \int^{T_{\rm tot}} |\delta\mathbf{R}(t_{\rm obs})|^2 dt_{\rm obs}}. \tag{5}$$

Similarly, if "δ" before Y or $\mathbf{R}$ in Equation 4 or 5 is replaced by "$\delta_{\rm s}$", "$\delta_{\rm p}$", or "$\delta_{\rm c}$", it means the RMS spin-induced perturbations, stellar perturbations or the combinations of them, respectively.

4. The Newtonian perturbations of a single perturber

In this section, we study the simple case that the target star orbiting the MBH is perturbed by a single perturber. The target star and the perturber are considered to be the currently detected ones (See Section 4.1), or those undetected, but very likely to be existed in the vicinity of the MBH in the GC (See Section 4.2). The importance of such analysis is mainly threefold: (1) As we will see in the latter sections, such studies help to understand the behaviors of the Newtonian perturbation and its difference with the spin-induced effects; (2) They help to reveal the Newtonian perturbations contributed by the individual perturber when the target star is embedded in a stellar cluster. (3) As currently there are relatively large uncertainties for the mass profiles in the vicinity of the MBH (See details in Section 5), it remain possible that a target star within a few hundred AU from the MBH is attracted by just a few perturbers located inside or nearby (See also Figure 8). In these cases, such a target star-perturber-MBH three body problem may be important if one of the perturbers among them play a dominant role in the signals of the Newtonian perturbations.

4.1. Perturbations on S2/S0-2 from S0-102

Among all of the currently detected S-stars, the star S2/S0-2 is of particular interests for testing the spin-induced effects. As it is in close proximity to the MBH and have relatively high

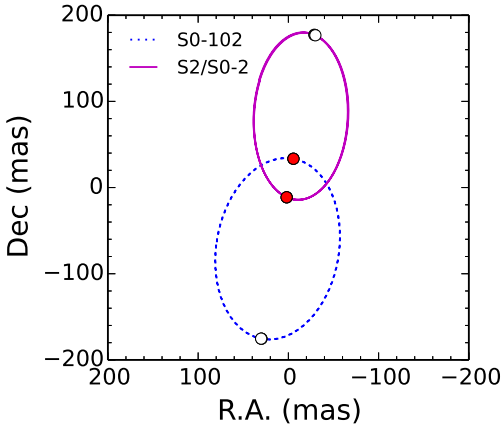

Fig. 1.— Apparent trajectories of S2/S0-2 (solid magenta line) and S0-102 (the dotted blue line) in the sky plane over three orbits. Red solid and white open circles mark the locations of the periapsis and apoapsis, respectively.

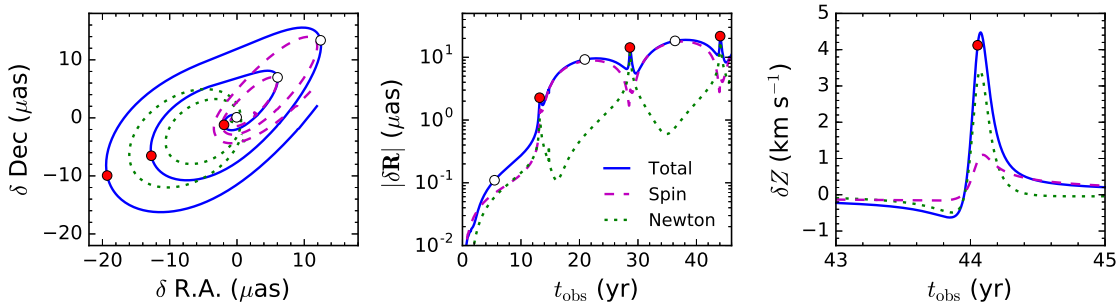

Fig. 2.— Perturbations on the apparent position [$\delta\mathbf{R} = (\delta\mathrm{R.A.}, \delta\mathrm{Dec})$, left panel], its distance in the sky plane ($|\delta\mathbf{R}|$, middle panel), and the redshift (δZ, right panel) of S2/S0-2 as a function of the observational time ($t_{\rm obs}$) in three orbits. Note that in the right panel, only the evolutions of δZ near the third pericenter passage of S2/S0-2 ($t_{\rm obs} \simeq 44.1$ yr) is plotted. In each panel, the perturbations on these signals of star S2/S0-2 are due to the spin-induced effects when $a = 0.99$, $i = 45^\circ$ and $\epsilon = 200^\circ$ (magenta dashed lines), the Newtonian attractions of S0-102 with $m_{\rm p} = 0.5 M_\odot$ (green dotted lines), and the combination effects of the above two (blue solid lines), all of which are obtained by the method described in Section 3. Red solid and white open circles mark the periapsis and apoapsis passage points of S2/S0-2, respectively.

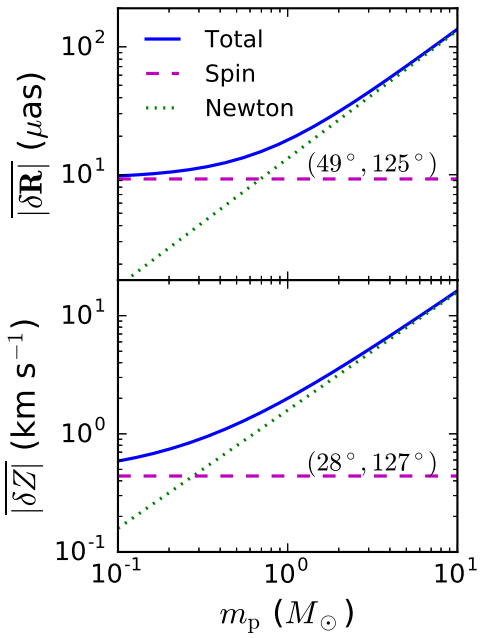

Fig. 3.— RMS values of the perturbations on the position signal ($\overline{|\delta \mathbf{R}|}$, top panel) or the redshift signal ($\overline{|\delta Z|}$, bottom panel) of S2/S0-2 over three orbits versus the mass of S0-102 ($m_{\rm p}$). In each panel, the perturbations are due to the spin-induced effects (magenta dashed line), the Newtonian attractions of S0-102 (green dotted line), and the combination effects of the above two (blue solid line). In the top panel, the spin orientation is $i = 49^\circ$ and $\epsilon = 125^\circ$, such that the spin-induced position displacement of S2/S0-2 are most significant; In the bottom panel, the spin orientation is $i = 28^\circ$ and $\epsilon = 127^\circ$, such that the spin-induced redshift difference of S2/S0-2 are most significant.

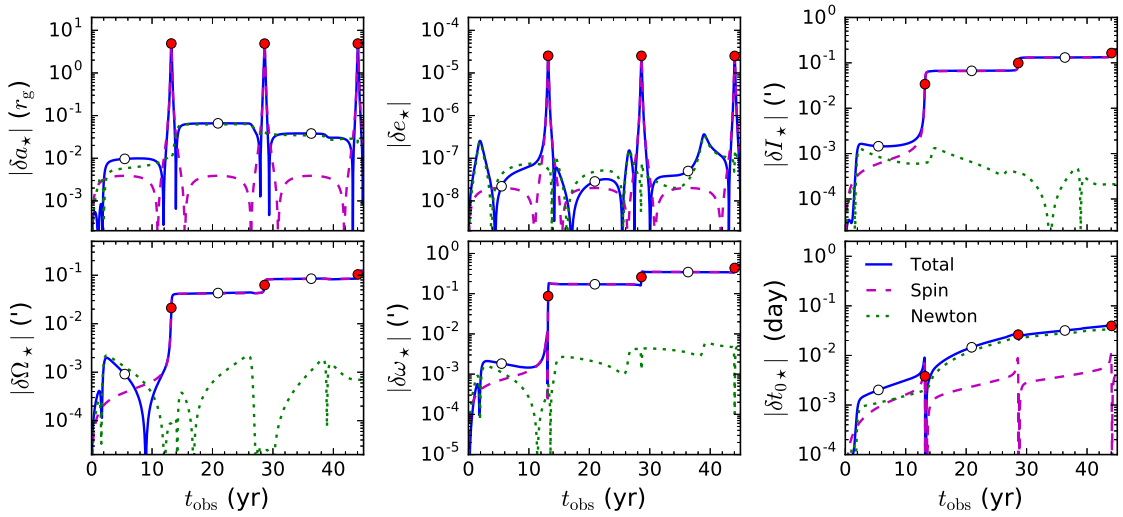

Fig. 4.— Perturbations on the six orbital elements of S2/S0-2, which are the orbital semimajor axis ($a_\star$, top left panel), eccentricity ($e_\star$, top middle panel), inclination ($I_\star$, top right panel), ascending node ($\Omega_\star$, bottom left panel), longitude of angle to periapsis ($\omega_\star$, bottom middle panel), and the time of pericenter passage ($t_{0\star}$, bottom right panel). In each panel, the perturbations are due to the spin-induced effects when $a = 0.99$, $i = 45°$ and $\epsilon = 200°$(magenta dashed line), the Newtonian attractions of S0-102 with $m_{\rm p} = 0.5 M_\odot$ (green dotted line), and the combination effects of the above two (blue solid line). Red solid and white open circles mark the periapsis and apoapsis passage points of S2/S0-2, respectively.

Table 1: Initial Orbital Elements of the Target stars and Perturbers.

Target star	$a_\star$ (AU)	$r_{\rm per,\star}$ [a] ($r_{\rm g}$)	$e_\star$	$I_\star$ (°)	$\Omega_\star$ (°)	$\omega_\star$ (°)	$t_{0\star}$ [b] (yr)	$f_\star$ (°)
S2/S0-2[c]	984	2993	0.88	135	225	63	2.32	–
T1[e]	$50-800$	$152-2434$	0.88	45	0	0	–	180
T2[e]	$50-800$	$887-14198$	0.3	45	0	0	–	180
Perturber	$a_{\rm p}$ (AU)	$r_{\rm per,p}$ [a] ($r_{\rm g}$)	$e_{\rm p}$	$I_{\rm p}$ (°)	$\Omega_{\rm p}$ (°)	$\omega_{\rm p}$ (°)	$t_{0\rm p}$ [b] (yr)	$m_{\rm p}$ ($M_\odot$)
S0-102[d]	848	6880	0.68	151	175	185	9.5	0.5
P1[f]	100	304	0.88	Ran	Ran	Ran	Ran	10
P2[f]	600	1825	0.88	Ran	Ran	Ran	Ran	10

Note. —

[a] Distance at pericenter.

[b] Time of the pericenter passage respective to the year of 2000.

[c] Taken from Gillessen et al. (2009).

[d] Taken from Meyer et al. (2012).

[e] The orbital semimajor axis ($a_\star$) adopts one of the ten values that are logarithmically spaced between 50 AU and 800 AU, which are 50 AU, 68 AU, 93 AU, 126 AU, 171 AU, 233 AU, 317 AU, 432 AU, 588 AU, and 800 AU. The distance at pericenter ($r_{\rm per,\star}$ in unit of $r_{\rm g} \simeq 0.04$ AU) of T1 and T2 can then be obtained correspondingly.

[f] In the MC simulation, $I_{\rm p}$, $\Omega_{\rm p}$, $\omega_{\rm p}$ of the perturber are with random values between 0° and 360°, $t_{0\rm p}$ of the perturber is with random values between 0 and $P(a_{\rm p})$, here $P(a_{\rm p})$ is the orbital period of the perturber.

eccentricity, the continuous monitoring of the orbital motion of S2 by the future facilities, i.e., TMT or E-ELT, can be used to provide constraints on the spin parameters of the MBH (See ZLY15). However, it requires a clean separation of the stellar perturbations caused by other surrounding S-stars or the still undetected stars/stellar remnants. One of the closest S-stars is the recently discovered S0-102, which has the shortest orbital period known so far (Meyer et al. 2012). It has been found that S0-102 is not particularly suited to probe the spin parameters of the MBH (See ZLY15), but it may introduce gravitational perturbations on the orbits of S2/S0-2. In this section, we study the perturbations on both the orbit elements and the direct observables of S2/S0-2 due to the gravitational pull from S0-102.

We adopt the initial conditions of the target star S2/S0-2 and the perturber S0-102 according to the recent observations (Gillessen et al. 2009; Meyer et al. 2012, see Table 1). We simulate the orbital motion of S2/S0-2 over three orbital periods, beginning in the year of 2020 (corresponding to $t_{\rm obs} = 0$), to mimic the observational signals probed by the future telescopes. As currently the mass of S0-102 is poorly known, we assume $m_{\rm p} = 0.5M_{\odot}$ for it. As we will see later in this section, such assumed mass of S0-102 result in Newtonian perturbations almost comparable with those caused by the spin-induced effects on both the position and redshift signals of the S2/S0-2. We will discuss the dependence of the results on the mass of S0-102 later in this section.

For the magnitude and direction of the MBH spin we assume three different cases: (1) $a = 0.99$, $i = 45^{\circ}$ and $\epsilon = 200^{\circ}$, such that both the spin-induced effects on the position and redshift signals of S2/S0-2 are modest; (2) $a = 0.99$, $i = 49^{\circ}$ and $\epsilon = 125^{\circ}$, such that the spin-induced position displacement of S2/S0-2 are most significant. (3) $a = 0.99$, $i = 28^{\circ}$ and $\epsilon = 127^{\circ}$, such that the spin-induced redshift differences of S2/S0-2 are most significant (See also Yu et al. 2016).

4.1.1. Perturbations on the observables of S2/S0-2

The simulated apparent trajectories of these two stars in the sky plane are showed in Figure 1. Figure 2 show the simulation results of the perturbations on the observables of S2/S0-2 due to the spin-induced effects when $a = 0.99$, $i = 45^{\circ}$ and $\epsilon = 200^{\circ}$ (dashed magenta lines), the Newtonian attractions of S0-102 (green dotted lines), and the combination effects of them (solid blue lines). Table 2 shows the maximum and the RMS values of these perturbations over the three orbits. The details of the results are discussed as follows.

The evolutions of the spin induced perturbations on the apparent position ($\delta_{\rm s}\mathbf{R}$), its distance in the sky plane ($|\delta_{\rm s}\mathbf{R}|$), and the redshift ($\delta_{\rm s}Z$) of S2/S0-2 are showed in the dashed magenta lines in left, middle and right panel of Figure 2, respectively. We can see that the spin-induced position displacement is spiral-like, mounts up and peaks near the apocenter in each orbit, while the spin-induced redshift difference is most variable and peaks near the pericenter in each orbit. Note that these spin-induced effects depend on the assumed spin orientations. The values of the

maximum and RMS spin-induced perturbations over three orbits in three cases of spin orientations are showed in Table 2.

The Newtonian perturbations on both the position and redshift signals of S2/S0-2 show quite different evolutions compared with those of the spin-induced effects (See the dotted green lines in Figure 2). The Newtonian perturbation on both position and redshift signals peak around the pericenter in each orbit, with the maximum values given by $|\delta_{\rm p}\mathbf{R}|_{\rm max} \sim 17.9\mu$as and $|\delta_{\rm p}Z|_{\rm max} \simeq 3.4$ km s^{-1} around the third pericenter passage. The corresponding RMS values are given by $\overline{|\delta_{\rm p}\mathbf{R}|} = 6.7\mu$as and $\overline{\delta_{\rm p}Z} = 0.8$ km s^{-1} for the apparent position and the redshift signals, respectively.

The combined perturbations of the Newtonian and the spin-induced effects are complex (See the blue solid lines in each panel of Figure 2), as in the simulations here they are comparable to each other, i.e., $\overline{|\delta_{\rm p}\mathbf{R}|} \simeq \overline{|\delta_{\rm s}\mathbf{R}|}$ or $\overline{|\delta_{\rm p}Z|} \simeq \overline{\delta_{\rm s}Z}$. Note that the combined perturbations on the position signal of S2/S0-2 show peaks both near the pericenter and apocenter, which are contributed by the Newtonian and the spin-induced effects, respectively.

Table 2: Perturbations on position and redshift of S2/S0-2 over three orbital periods

(i,ϵ) [1]	$\lvert\delta_{\rm s}\mathbf{R}\rvert_{\rm max}$ [2]	$\lvert\delta_{\rm p}\mathbf{R}\rvert_{\rm max}$ [3]	$\lvert\delta_{\rm c}\mathbf{R}\rvert_{\rm max}$ [4]	$\overline{\lvert\delta_{\rm s}\mathbf{R}\rvert}$ [5]	$\overline{\lvert\delta_{\rm p}\mathbf{R}\rvert}$ [6]	$\overline{\lvert\delta_{\rm c}\mathbf{R}\rvert}$ [7]	$\lvert\delta_{\rm s}Z\rvert_{\rm max}$ [8]	$\lvert\delta_{\rm p}Z\rvert_{\rm max}$ [9]	$\lvert\delta_{\rm c}Z\rvert_{\rm max}$ [10]	$\overline{\lvert\delta_{\rm s}Z\rvert}$ [11]	$\overline{\lvert\delta_{\rm p}Z\rvert}$ [12]	$\overline{\lvert\delta_{\rm c}Z\rvert}$ [13]	$m_{\rm p}^{\rm zc}$ [14]	$m_{\rm p}^{\rm rc}$ [15]
$(45^\circ, 200^\circ)$	17.8	17.9	22.3	6.1	6.7	10.5	1.1	3.4	4.4	0.32	0.79	1.1	0.45	0.20
$(49^\circ, 125^\circ)$	26.5	17.9	27.2	9.3	6.7	13.1	1.5	3.4	4.9	0.41	0.79	1.2	0.69	0.26
$(28^\circ, 127^\circ)$	24.8	17.9	25.7	8.5	6.7	12.5	1.6	3.4	5.0	0.44	0.79	1.2	0.64	0.28

Note. — Summaries of the perturbations on position and redshift signals of S2/S0-2 over three orbital periods. Col.[1]: i and ϵ are the two angles defining the spin orientation: i is the line of sight inclination of the spin, ϵ is the angle between the projection of the direction of the spin onto the sky plane and a reference direction (See Figure 1 in ZLY15). Col.[2-7]: The maximum (Col.[2-4]) and RMS values (Col.[5-7]) of the perturbations on the position signal of S2/S0-2 over three orbits, in units of μas. Col.[8-13]: The maximum (Col.[8-10]) and RMS values (Col.[11-13]) of the perturbations on the redshift signal of S2/S0-2 over three orbits, in units of km s^{-1}. In Col.[2-13], the quantities with "$\delta_{\rm s}$", "$\delta_{\rm p}$", and "$\delta_{\rm c}$" mean the perturbations due to spin-induced effects, the Newtonian attractions of S0-102 with $m_{\rm p} = 0.5 M_\odot$, and the combination effects of them, respectively. Col.[14-15]: $m_{\rm p}^{\rm rc}$ is the mass of S0-102 when $\overline{\lvert\delta_{\rm p}\mathbf{R}\rvert} = \overline{\lvert\delta_{\rm s}\mathbf{R}\rvert}$; $m_{\rm p}^{\rm zc}$ is the mass of S0-102 when $\overline{\lvert\delta_{\rm p}Z\rvert} = \overline{\lvert\delta_{\rm s}Z\rvert}$.

We find that the Newtonian perturbations are proportional to the mass of S0-102 ($m_{\rm p}$), as showed in the dotted green lines in Figure 3. The RMS Newtonian perturbation are given by $\overline{|\delta_{\rm p}\mathbf{R}|} \simeq 13.4\,(m_{\rm p}/1M_\odot)\mu$as and $\overline{\delta_{\rm p}Z} \simeq 1.6\,(m_{\rm p}/1M_\odot)$ km s^{-1} for the position and redshift signals of S2/S0-2, respectively. Thus, there is a critical mass of S0-102, i.e., $m_{\rm p}^{\rm rc}$ (or $m_{\rm p}^{\rm zc}$), when the RMS value of the Newtonian perturbations on position (or redshift) signal is equal to those resulting from the spin-induced effects, i.e., $\overline{|\delta_{\rm p}\mathbf{R}|} = \overline{|\delta_{\rm s}\mathbf{R}|}$ (or $\overline{\delta_{\rm p}Z} = \overline{\delta_{\rm s}Z}$). The spin effects in position (or redshift) of S2/S0-2 will be obscured by the Newtonian perturbations if $m_{\rm p} > m_{\rm p}^{\rm rc}$ (or $m_{\rm p} > m_{\rm p}^{zc}$). The critical masses in the cases of different spin orientations are showed in Table 2. When the spin-induced effects become most significant, we get the upper limit of the critical mass, i.e., $m_{\rm p}^{\rm rc} = 0.7M_\odot$ and $m_{\rm p}^{\rm zc} = 0.28M_\odot$, for the position and redshift signals of S2/S0-2, respectively. As the S-stars are exclusively B-type main-sequence stars with masses $\gtrsim 3M_\odot$ (Ghez et al. 2008; Gillessen et al. 2009), S0-102 is likely more massive than these critical values. Thus, it is quite plausible that the spin-induced signals of S2/S0-2 are obscured by the perturbations from S0-102 alone.

Observationally, the spin-induced effects can be measured by subtracting the stellar perturbations from the total measured shifts. In the case of S0-102, they may be well removed in the ideal case when it is the only S-star closer to the MBH than S2/S0-2, and if the orbital parameters and the mass of S0-102 are observationally determined. The difference between the spin-induced effects and the stellar perturbations from S0-102 may provide helpful hints on discerning them from the observational data.

4.1.2. Perturbations on the orbital elements of S2/S0-2

The standard osculating orbital elements of stars are instantaneously calculated from the values of their position and velocity vectors from usual Keplerian formulas. Here we calculate the orbital elements of S2/S0-2 by the three-position and the three-velocity in its LNRF frame (See Eq. 9-11 in ZLY15). Both the Newtonian perturbations from S0-102 and the relativistic spin-induced effects induce variations of the orbital elements of S2/S0-2. The perturbations on the observables, i.e., $\delta\mathbf{R}$ and δZ, are approximately related to the variations of the orbital elements by

$$\delta\mathbf{R}(t_{\rm obs}) \simeq \sum_{\kappa} \frac{\partial \mathbf{R}}{\partial \kappa}\delta\kappa(t_{\rm obs}), \tag{6}$$

and

$$\delta Z(t_{\rm obs}) \simeq \sum_{\kappa} \frac{\partial Z}{\partial \kappa}\delta\kappa(t_{\rm obs}), \tag{7}$$

respectively, where $\kappa = a_\star$, $e_\star$, $I_\star$, $\Omega_\star$, $\omega_\star$ and $t_{0\star}$ (or $f_\star$). We calculate the perturbations on the orbital elements of S2/S0-2 according to the method described in Section 3. The results in the case that $a = 0.99$, $i = 45^\circ$ and $\epsilon = 200^\circ$ are depicted in Figure 4 and discussed as follows (The results for other two spin orientations are similar).

The spin-induced effects cause the variations of all the orbital elements (See the magenta dashed lines in Figure 4). The perturbations on the semimajor axis $|\delta_{\rm s}a_\star|$ and eccentricity $|\delta_{\rm s}e_\star|$ due to the spin-induced effects oscillate periodically, with local maximums at both periapsis and apoapisis. The orbit-averaged values of $\delta_{\rm s}a_\star$ and $\delta_{\rm s}e_\star$ remain constant as a function of time. Due to the frame-dragging and also other high order GR effects, $\delta_{\rm s}I_\star$, $\delta_{\rm s}\Omega_\star$, and $\delta_{\rm s}\omega_\star$ increase with time. At the third pericenter, the variations of these orbital elements amount to $\delta_{\rm s}I_\star = 0.16'$, $\delta_{\rm s}\Omega_\star = -0.10'$, and $\delta_{\rm s}\omega_\star = -0.44'$. The time of pericenter passage $\delta_{\rm s}t_{0\star}$ (or similarly, $\delta_{\rm s}f_\star$) increases also slightly at each orbit, as the orbital period of the star orbiting a MBH with, and without spinning, is different. One can show that the spin-induced position difference $|\delta_{\rm s}\mathbf{R}|$ and $\delta_{\rm s}Z$ are contributed by both the orbital precession ($\delta_{\rm s}I_\star$, $\delta_{\rm s}\Omega_\star$ and $\delta_{\rm s}\omega_\star$) and also the $\delta_{\rm s}t_{0\star}$ (or $\delta_{\rm s}f_\star$) (See also Yu et al. 2016; ZLY15).

The gravitational attractions of S0-102 can also cause changes of all the orbital elements of S2/S0-2 (See the green dotted lines in Figure 4). We find that the stellar perturbations on the orbital elements are complex and quite different from the spin-induced relativistic ones. Particularly, we found that the orbit-averaged Newtonian perturbations on the orbital semimajor axis do not remain constant but vary after each orbit. At the third pericenter, the variations of the elements of S2/S0-2 are given by $\delta_{\rm p}a_\star \simeq 0.03r_{\rm g}$, $\delta_{\rm p}e_\star \simeq \underset{\sim\sim}{10^{-7}}$, $\delta_{\rm p}I_\star \simeq 0.014''$, $\delta_{\rm p}\Omega_\star \simeq 0.041''$, $\delta_{\rm p}\omega_\star \simeq -0.0035''$ and $\delta_{\rm p}t_{0\star} \simeq 0.034$day (or $\delta_{\rm p}f_\star = -4.3'$). As $\delta_{\rm p}I_\star \ll \delta_{\rm s}I_\star$, $\delta_{\rm p}\Omega_\star \ll \delta_{\rm s}\Omega_\star$, $\delta_{\rm p}\omega_\star \ll \delta_{\rm s}\omega_\star$, the Newtonian orbital precessions are negligible compared to the relativistic spin-induced ones. As showed by the analytical calculations below, it turns out that the Newtonian perturbations on the observables, $|\delta_{\rm p}\mathbf{R}|$ and $\delta_{\rm p}Z$, are mainly explained by perturbed orbital periods (or $\delta_{\rm p}f_\star$), rather than the Newtonian orbital precessions.

The changes of the orbital semimajor axis, i.e., $\delta_{\rm p}a_\star$, due to the Newtonian attractions of S0-102, cause variations of the orbital period and the time of arrival in each point in the orbit of the target star. Suppose that the evolution of the true anomaly of the S2/S0-2 with and without perturbations of S0-102 are given by $f'_\star(t'_\star)$ and $f_\star(t_\star)$, respectively, then when the star reach to the same true anomaly, i.e., $f'(t'_\star) = f(t_\star)$, the difference of the time of arrival in these two cases is given by $\delta_{\rm p}t_\star = t'_\star - t_\star$. If we assume that the perturbation is small, i.e., $df'(t_\star)/dt_\star \simeq df(t_\star)/dt_\star$, then at a given moment $t_\star$, the difference of the true anomaly is given by

$$\begin{aligned}\delta_{\rm p}f_\star(t_\star) &= f'_\star(t_\star) - f_\star(t_\star) \\ &\simeq -\frac{df_\star}{dt_\star}\delta_{\rm p}t_\star \simeq -\frac{\sqrt{M_\bullet G a_\star(1-e_\star^2)}}{r^2}\delta_{\rm p}t_\star.\end{aligned} \tag{8}$$

At the pericenter, we simply have $\delta_{\rm p}t_\star = \delta_{\rm p}t_{0\star}$. Then the variation of the true anomaly is given by

$$\delta_{\rm p}f_\star \simeq -\frac{v_{\rm per}}{a_\star(1-e_\star)}\delta_{\rm p}t_{0\star}. \tag{9}$$

Here $v_{\rm per} = \sqrt{\frac{M_\bullet G}{a_\star}}\sqrt{\frac{1+e_\star}{1-e_\star}}$ is the velocity of the star at the pericenter. Note that if substituting the simulation result $\delta_{\rm p}t_{0\star} = 0.034$day to Equation 9, we have $\delta_{\rm p}f_\star = -4.3'$, which is also consistent

with the result of the simulation.

At the third pericenter, the resulting position displacement and difference of the velocity in the line of sight (which can be approximately regarded as the redshift) due to the perturbed period (or the variations of $f_\star$) are given by

$$\begin{aligned} |\delta_{\rm p}\mathbf{R}|_{f_\star=0} &\simeq a_\star(1-e_\star)(1-\cos^2\omega_\star\sin^2 I_\star)^{1/2}|\delta_{\rm p}f_\star| \\ &\simeq 17.8\mu{\rm as} \end{aligned} \tag{10}$$

and

$$\begin{aligned} |\delta_{\rm p}Z|_{f_\star=0} &\simeq \sqrt{\frac{GM_\bullet}{a_\star(1-e_\star^2)}}\sin\omega_\star\sin I_\star|\delta_{\rm p}f_\star| \\ &\simeq 3.2\ {\rm km\ s^{-1}}, \end{aligned} \tag{11}$$

respectively. This analysis is well consistent with the numerical simulation results, i.e., $|\delta_{\rm p}\mathbf{R}| \simeq 17.9\mu$as and $|\delta_{\rm p}Z| \simeq 3.4$ km s^{-1}, at the third pericenter of S2/S0-2 (See Table 2).

Similarly, we can obtain the analytical expressions of $|\delta_{\rm p}\mathbf{R}|$ and $|\delta_{\rm p}Z|$ for arbitrary $f_\star$. Note that according to Equation 8, $\delta_{\rm p}f_\star$ peaks around the pericenter in each orbit, thus the resulting perturbations on the observables of S2/S0-2 also peak around the pericenter (See Section 4.1.1 and Figure 2).

Meanwhile, we find that the Newtonian orbital precessions induce negligible changes on the observables of S2/S0-2. According to Equation 6 and 7, near the third pericenter passage, the changes of the observables due to the Newtonian orbital precessions are given by (Similar to Equation 31 and 36 in ZLY15)

$$\begin{aligned} |\delta_{\rm p}\mathbf{R}|_{\rm prec} \simeq a_\star(1-e_\star)\,\big[&\delta_{\rm p}^2\Omega_\star(1-\sin^2\omega_\star\sin^2 I_\star) \\ &+\delta_{\rm p}^2\omega_\star(1-\cos^2\omega_\star\sin^2 I_\star) \\ &+\sin^2\omega_\star\sin^2 I_\star\delta_{\rm p}^2 I_\star + 2\cos I_\star\delta_{\rm p}\Omega_\star\delta_{\rm p}\omega_\star \\ &-2\sin\omega_\star\cos\omega_\star\sin I_\star\cos I_\star\delta_{\rm p}\omega_\star\delta_{\rm p}I_\star \\ &-2\sin\omega_\star\cos\omega_\star\sin I_\star\delta_{\rm p}\Omega_\star\delta_{\rm p}I_\star\big]^{1/2} \\ \simeq\ & 0.03\mu{\rm as} \end{aligned} \tag{12}$$

and

$$\begin{aligned} |\delta_{\rm p}Z|_{\rm prec} \simeq \sqrt{\frac{GM_\bullet}{a_\star(1-e_\star^2)}}(1+e_\star)\,&(\cos\omega_\star\cos I_\star\delta_{\rm p}I_\star \\ &-\sin\omega_\star\sin I_\star\delta_{\rm p}\omega_\star) \\ \simeq\ & 10^{-3}\ {\rm km\ s^{-1}}, \end{aligned} \tag{13}$$

for the position and redshift signals, respectively. These values are orders of magnitude lower than those in Equation 10 and 11.

Similarly, for most of the simulations performed in the latter sections, i.e., in which a generic target star is perturbed by a single (Section 4.2) or multiple disturbing objects (Section 5), we find

that the Newtonian perturbations on the observables are mainly caused by the perturbed orbital periods of the target star, rather than the Newtonian orbital precessions. Only in some rare cases, that the perturber is with some particular orbital configurations, the effects due to the perturbed orbital period are smaller than those of the Newtonian orbital precessions.

4.1.3. Comparing with the PN simulations

The orbital elements of the target star are defined according to its simultaneous position and velocity. Thus, the signals of the Newtonian perturbations on them may show different behaviours if the adopted spacetime metric is different. It would be interesting to compare the Newtonian perturbations on the orbital elements resulting from our simulations with those from the post-Newtonian (PN) numerical simulations. Here, with the same initial conditions, we implement the PN numerical simulations to calculate the orbital evolutions of S2/S0-2 due to the gravitational attractions of S0-102. We adopt the PN formalism in Kidder (1995) up to 2.0 order and ignore the spin-related PN terms. For both the simulations adopting PN formalism and the method in this work, we extract the effects of the Newtonian attraction of S0-102 from the total effects by examining the differences of the orbital elements when we turn the Newtonian gravity of S0-102 on and then off (See the extraction method described in Section 3).

The comparisons between results of the PN simulation and those of this work are showed in Figure 5. We can see that these two methods predict almost the same evolutions of the perturbations, especially for some of the orbital elements, i.e., $I_\star$, $\Omega_\star$ and $t_{0\star}$. For the other elements defined in the orbital plane, i.e. $a_\star$, $e_\star$ and $\omega_\star$, there is a relatively large discrepancy near each pericenter passage. Such differences can be explained by the fact that the spacetime metric in the PN simulations is based on the weak field approximation, while here we use the pure Kerr metric. Nonetheless, we find that they lead to only a negligible difference in the overall effects of the Newtonian attractions of S0-102. For example, after three orbital evolution, the relative difference of the Newtonian perturbations on the orbital elements obtained from this work ($\delta_{\rm p}\kappa_{\rm hm}$) and those from the PN simulations ($\delta_{\rm p}\kappa_{\rm pn}$) is about $|\frac{\delta_{\rm p}\kappa_{\rm hm}-\delta_{\rm p}\kappa_{\rm pn}}{\delta_{\rm p}\kappa_{\rm pn}}| \lesssim 10^{-2}$, here κ is any orbital elements of S2/S0-2. The PN simulations result in $\delta_{\rm p}f \simeq -4.2'$ at the third pericenter. By Equation 10 and 11 we find that the resulting perturbations are given by $|\delta_{\rm p}\mathbf{R}|_{f_\star} \simeq 17.5\mu$as and $|\delta_{\rm p}Z|_{f_\star} \simeq 3.1$ km s^{-1}, which are consistent with those from our method. However, the PN simulations consider only the orbital variations in the local frame of the star. As we additionally include the light tracing technique, our simulation has the power of predicting the stellar perturbations on the direct observables of the target star, which are also the main focus of this study.

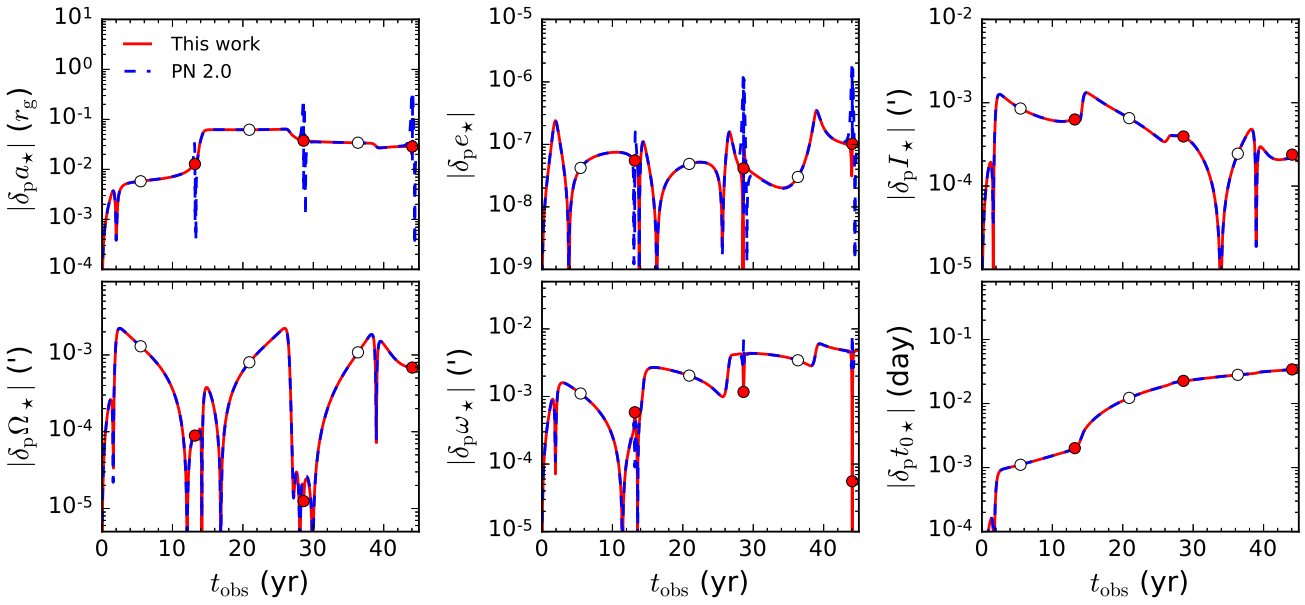

Fig. 5.— Perturbations on the six orbital elements of S2/S0-2 due to the Newtonian attractions of S0-102, obtained by post-Newtonian numerical simulations with 2.0 order corrections (blue dashed lines) or the method presented in this work (red solid lines). The mass of S0-102 is assumed to be $m_{\rm p} = 0.5 M_\odot$. Red solid and white open circles mark the periapsis and apoapsis passage points of S2/S0-2, respectively.

4.2. The perturbations on a hypothetical S-star

It is plausible that some currently undetected S-stars are located inside the orbit of S2/S0-2 or S0-102 in the GC, which may be revealed by the future facilities (e.g., Zhang et al. 2013). These S-stars are better GR probes than S2/S0-2 and may be able to put tight constraints on the spin parameters (e.g., Angélil et al. 2010; ZLY15). Similarly to S2/S0-2, these S-stars are likely to be disturbed by other surrounding stars or stellar remnants, and such perturbations should be carefully handled for the unbiased measurements of the spin-induced effects. By performing a large number of Monte Carlo (MC) simulations, here we study the case that a hypothetical S-star located inside the orbits of S2/S0-2 or S0-102 ($\lesssim$ 800 AU) is perturbed by a single perturber. As these stars are currently undetected, for both the target star and the perturber we consider various initial conditions of them. The details of the simulations and the results are showed in the following sections.

4.2.1. The Monte Carlo Simulations

We explore the problem by performing the MC numerical simulations as follows: We consider a target star with $a_\star$ takes a value between 50 AU to 800 AU, $e_\star = 0.88$ (The star T1) or $e_\star = 0.3$ (The star T2). For each target star, we perform $N_{\rm MC} = 100$ MC simulations in which it is perturbed by a perturber with randomly selected values of $I_{\rm p}$, $\Omega_{\rm p}$, $\omega_{\rm p}$ and $t_{0{\rm p}}$[3] over three orbits. The orbital semimajor axis of the perturber in these MC simulations are $a_{\rm p} = 100$ AU (The perturber P1) or 600 AU (The perturber P2). The initial conditions of the target stars and the perturbers are listed in Table 1. We estimate the log-average value of the RMS position displacement in these MC simulations, i.e., $\langle\overline{|\delta\mathbf{R}|}\rangle$, by

$$\log\langle\overline{|\delta\mathbf{R}|}\rangle = \sum_{j}^{N_{\rm MC}} \frac{\log\overline{|\delta\mathbf{R}|}_j}{N_{\rm MC}}, \tag{14}$$

here $N_{\rm MC} = 100$, $|\delta\mathbf{R}|_j$ is the RMS perturbations on the position signal in the j-th MC simulation. Similarly, we can define the log-average value for the redshift signal, i.e., $\langle\overline{\delta Z}\rangle$, or any other quantities of the target star. The simulation results of $\langle\overline{|\delta_{\rm p}\mathbf{R}|}\rangle$ and $\langle\overline{\delta_{\rm p} Z}\rangle$ for the target star T1 and T2 are showed in Figure 6 and 7, respectively. The associated error bars show the standard deviations (about $1-1.5\,$dex) due to the randomly selected initial values of $\Omega_{\rm p}, \Upsilon_{\rm p}, I_{\rm p}$ and $t_{0{\rm p}}$. Note that for the spin-induced signals, we simply have $\langle\overline{|\delta_{\rm s}\mathbf{R}|}\rangle = \overline{|\delta_{\rm s}\mathbf{R}|}$ and $\langle\overline{\delta_{\rm s} Z}\rangle = \overline{\delta_{\rm s} Z}$.

[3] We find that the Newtonian perturbations depend complexly on the the parameter $I_{\rm p}$, $\Omega_{\rm p}$, $\omega_{\rm p}$ and $t_{0{\rm p}}$ of the perturber. Here we randomize them as we do not have particular interests in the details of the dependence on these parameters but focus only on their average effects of the Newtonian perturbations.

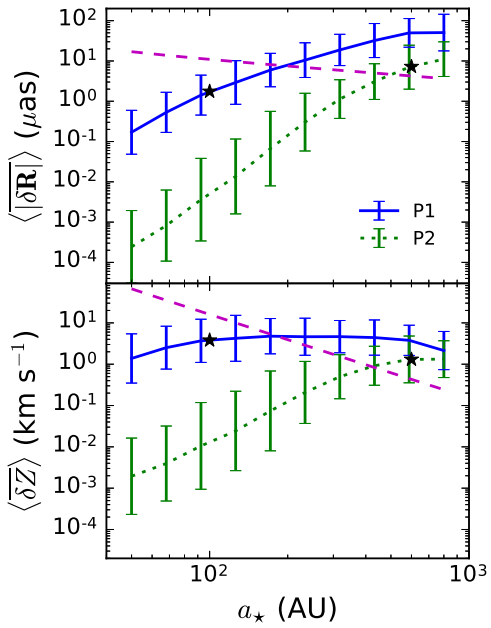

Fig. 6.— Top panel: Perturbations on the apparent position of the target star T1 (with $e_\star = 0.88$, see Table 1) as a function of $a_\star$. Here $\langle\overline{|\delta\mathbf{R}|}\rangle$ is the log-average value of the RMS position displacement of the target star in 100 MC simulations (See Equation 14). In each MC simulation, the target star is perturbed by a single perturber with randomly selected values of $I_{\rm p}$, $\Omega_{\rm p}$, $\omega_{\rm p}$ and $t_{0\rm p}$. The blue solid and green dotted lines show the simulation results of $\langle\overline{|\delta_{\rm p}\mathbf{R}|}\rangle$ when the perturber is with $a_{\rm p} = 100$ AU (the perturber P1) and $a_{\rm p} = 600$ AU (the perturber P2), respectively. The associated error bars are the standard deviations. The initial orbital elements of target stars and perturbers are showed in Table 1. The magenta dashed line shows the RMS spin-induced position displacement ($\overline{|\delta_{\rm s}\mathbf{R}|}$) in the case that $a = 0.99$, $i = 45°$, and $\epsilon = 180°$. The black star symbol in each line marks the location where $a_\star = a_{\rm p}$. Bottom panel: Similar to the top panel, but for the stellar perturbations on the redshift of the target star ($\langle\overline{\delta Z}\rangle$).

4.2.2. Results

From Figure 6 and 7, it appears that the scaling of $\langle|\overline{\delta_{\rm p}\mathbf{R}}|\rangle$ with $a_\star$ is different from those of $\langle\overline{\delta_{\rm p}Z}\rangle$. Such difference can be explained as follows. According to Section 4.1.2, the RMS Newtonian perturbations on the observables are related to the perturbations on the true anomaly of the target star by $\overline{|\delta_{\rm p}\mathbf{R}|} \propto a_\star\overline{\delta_{\rm p}f_\star}$ and $\overline{\delta_{\rm p}Z} \propto a_\star^{-1/2}\overline{\delta_{\rm p}f_\star}$, (See Equation 10, and 11). After averaging the different MC runs, we have $\langle\overline{|\delta_{\rm p}\mathbf{R}|}\rangle \propto a_\star\langle\overline{\delta_{\rm p}f_\star}\rangle$ and $\langle\overline{\delta_{\rm p}Z}\rangle \propto a_\star^{-1/2}\langle\overline{\delta_{\rm p}f_\star}\rangle$. Here $\langle\overline{\delta_{\rm p}f_\star}\rangle$ is the log-average value estimated by method similar to Equation 14. Thus, $\langle\overline{|\delta_{\rm p}\mathbf{R}|}\rangle \propto a_\star^{3/2}\langle\overline{\delta_{\rm p}Z}\rangle$, i.e., the scaling relations of these two signals are different by a factor of $a_\star^{3/2}$.

The Newtonian perturbations depend on the relative location of the perturber from the target star. From Figure 6 and 7, a perturber impose stronger Newtonian perturbations on the observables of a target star located around or outside of its orbit ($a_\star \gtrsim a_{\rm p}$), than that located inside of its orbit ($a_\star \lesssim \lambda a_{\rm p}$, $\lambda = 0.5 \sim 0.8$ is a factor determined by the simulations). For target stars located inside the orbit of the perturber, the Newtonian perturbations are increasing functions of $a_\star$. For example, in Figure 6, for the perturber with $a_{\rm p} = 600$ AU (the green dotted lines), $\langle\overline{|\delta_{\rm p}\mathbf{R}|}\rangle$ increases from $2.5 \times 10^{-4}\mu$as to 3.1μas, and $\langle\overline{|\delta_{\rm p}Z|}\rangle$ increases from 0.002 km s^{-1} to 0.9 km s^{-1}, if the $a_\star$ of the target star increases from 50 AU to 432 AU.

The Newtonian perturbations depend on other parameters of the target star and the perturber, which we describe them briefly here: (1) Both the Newtonian perturbation and the spin-induced effects strongly depend on the eccentricity of the target star. From Figure 6 and 7, we can see that the target stars with $e_\star = 0.3$ felt much smaller spin-induced effects and Newtonian perturbations than those target stars with $e_\star = 0.88$. (2) The Newtonian perturbations are proportional to the mass of the perturber, i.e., $\langle\overline{|\delta_{\rm p}\mathbf{R}|}\rangle \propto m_{\rm p}$ and $\langle\overline{|\delta_{\rm p}Z|}\rangle \propto m_{\rm p}$ (See also Section 4.1 or Figure 3). We find that such relation remain true if the mass of the perturber is in the range of $0.1M_\odot < m_{\rm p} < 100M_\odot$. (3) The average values of stellar perturbations depend weakly on the eccentricity of the perturber, i.e., $e_{\rm p}$. For example, if the eccentricities of the perturbers in the MC simulations of Figure 6 and 7 are replaced by $e_{\rm p} = 0.3$, we find that the results are quite similar. (4) The Newtonian perturbations depend complexly on other parameters related to the orbital configurations of the target star, i.e., $I_\star$, $\Omega_\star$, $\omega_\star$ and $f_\star$. We found that the Newtonian perturbations may differ by a factor of several to one order of magnitude if adopting different values of these parameters.

We can see that the Newtonian perturbations by a $10M_\odot$ perturber is already large enough to obscure the spin-induced signals. For the simulations showed in Figure 6 and 7, the spin-induced effects on the apparent position (or the redshift) can be drowned by the Newtonian perturbations if the orbital semimajor axis of the target star is larger than $260 \sim 500$ AU (or $200 \sim 430$ AU).

5. The Newtonian perturbations of a star cluster

Currently, the mass distribution within milli-parsec scale in the GC along with its actual composition remain largely uncertain. The infrared imaging and spectroscopic observations in the past two decades have revealed over thousands of brightest stars in the inner parsec distance (e.g., Genzel et al. 2010; Schödel et al. 2009). Most of these observed stars can be classified into two distinctive categories: (1) The early-type stars, which are the young ($\sim$ 10Myr), massive ($\gtrsim 7M_{\odot}$) and main-sequence O-type or B-type stars. Although these stars are rare (numbers of about several hundred, e.g., Paumard et al. 2006), they dominate the total luminosity within the inner parsec of the GC. (2) The late-type stars, which are old (several Gyrs), K-type or M-type giant stars with masses $1 \sim 2M_{\odot}$. These stars dominate the total star counts observed in the inner parsec of the GC. Due to their long lifetime, it is believed that they are the most promising tracers of the stellar distributions in the GC.

The proper motion observations of the late-type stars suggest that the extended mass within one parsec from the GC is given by $0.5 \sim 1.5 \times 10^6 M_{\odot}$ (e.g., Schödel et al. 2009). However, the radial distributions of the extended mass are not well constrained. Theoretical works expect that if the stars around the MBH are dynamically relaxed by two body interactions, cusp profiles should appear, i.e., $n(r) \propto r^{-\gamma}$, with $\gamma = 3/2 \sim 7/4$ (Bahcall & Wolf 1976, 1977). However, recent observations of the late-type stars suggest a flattened core-like profiles with $\gamma = 0 \sim 1$ towards the inner region (e.g., Do et al. 2009; Buchholz et al. 2009; Bartko et al. 2010; Do et al. 2013a,b). The deficit of the inner stars is currently not well understood. It may suggest that stars/stellar remnants in the inner parsec are not in the equilibrium state, or a significant number of the late-type stars in this region are destroyed by stellar collisions (e.g., Alexander 1999; Freitag et al. 2006; Dale et al. 2009).

It is expected that a cluster of stellar mass black holes (with masses of $\sim 10M_{\odot}$) may exist in the vicinity of the MBH, if the two-body relaxation time is less than a few Gyr in the GC (Hopman & Alexander 2006; Alexander & Hopman 2009). The stellar mass black holes may form by the collapses and explosions of the early-type stars at the end of their main-sequence lives, which later concentrate towards the center through mass segregation (e.g., Freitag et al. 2006). However, so far it remains largely unclear whether they dominate the mill-parsec scales.

Due to the large uncertainties in this region, we explore the stellar perturbations on the observables of a target star surrounded by a star cluster with some possible mass distributions and its composition. The details of the simulations and the results are showed in the following sections.

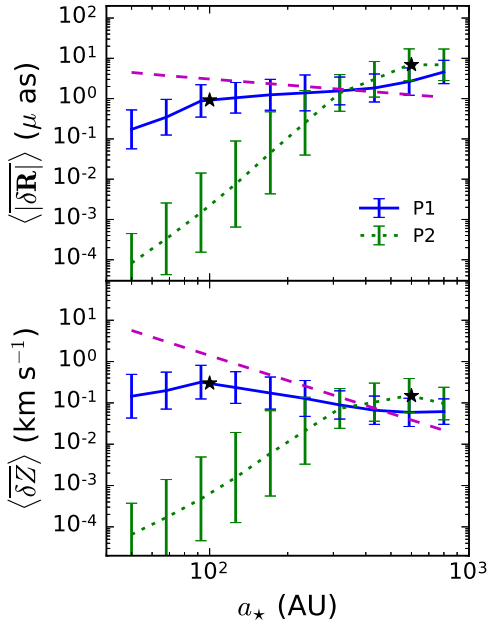

Fig. 7.— Legends similar to those for the Figure 6, but for the target star T2 (with $e_\star = 0.3$, see Table 1).

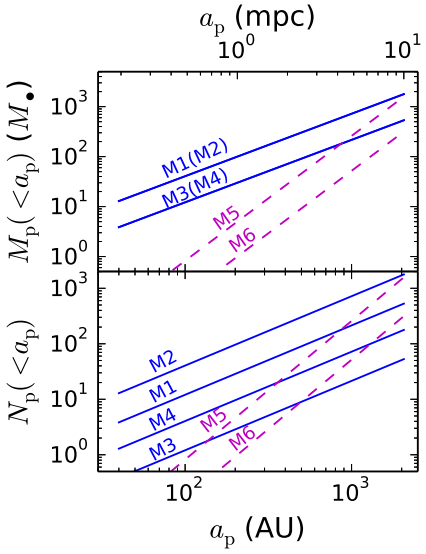

Fig. 8.— Total mass [$M_{\rm p}(< a_{\rm p})$, top panel] and number [$N_{\rm p}(< a_{\rm p})$, bottom panel] of perturbers with semimajor axis smaller than $a_{\rm p}$ for clusters in different models. The blue solid and the magenta dashed lines correspond to the models with the Bahcall-Wolf profiles ($\gamma = 7/4$, model M1-M4) and the core-like profiles ($\gamma = 0.5$, model M5-M6), respectively.

Table 3: Parameters of the Clusters in Different Models.

Model	$M_{\rm p}$	M_1	γ	β	$m_{\rm p}$	$N_{\rm p}$	$N_{\rm MC}$
	[1]	[2]	[3]	[4]	[5]	[6]	[7]
M1	1780	100	1.75	0.5	10	178	80
M2	1780	100	1.75	0.5	1	1780	8
M3	530	30	1.75	0.5	10	53	280
M4	530	30	1.75	0.5	1	530	28
M5	1581	5	0.5	-0.5	1	1581	10
M6	316	1	0.5	-0.5	1	316	48

Note. — The initial conditions of the clusters in different models. Col.[1]: The total mass of the cluster in units of $M_\odot$. Note that the perturbers in the clusters are with 40 AU $< a_{\rm p} <$ 2062 AU (0.2 mpc $\lesssim a_{\rm p} \lesssim$ 10 mpc); Col.[2]: Total mass of the perturbers with 0.2 mpc $\lesssim a_{\rm p} \lesssim$ 1 mpc, i.e., $M_1 = M_{\rm p}(< 1$ mpc), in units of $M_\odot$; Col.[3]: Slope of the density profile, i.e., $n(r) \propto r^{-\gamma}$; Col.[4]: The velocity anisotropy, given by $\beta = 1-\sigma_{\rm tr}^2/\sigma_{\rm los}^2$, here $\sigma_{\rm tr}$ and $\sigma_{\rm los}$ is the velocity dispersion in the transverse and the line of sight direction, respectively; Col.[5]: The mass of the perturber in units of $M_\odot$; Col.[6]: The total number of the perturbers in the cluster, i.e., $N_{\rm p} = M_{\rm p}/m_{\rm p}$; Col.[7]: The total number of MC simulations.

Table 4: Critical Values of the Target Stars in Different Models.

Model	$e_\star = 0.88$				$e_\star = 0.3$			
	$a_\star^{\rm rc}$	$r_{{\rm per},\star}^{\rm rc}$	$a_\star^{\rm zc}$	$r_{{\rm per},\star}^{\rm zc}$	$a_\star^{\rm rc}$	$r_{{\rm per},\star}^{\rm rc}$	$a_\star^{\rm zc}$	$r_{{\rm per},\star}^{\rm zc}$
	[1]	[2]	[3]	[4]	[5]	[6]	[7]	[8]
M1	120	360	100	300	100	1770	110	1950
M2	170	520	130	400	110	1950	120	2130
M3	170	520	130	400	130	2310	150	2660
M4	230	700	170	520	170	3020	190	3370
M5	270	820	200	610	200	3550	210	3730
M6	390	1190	330	1000	300	5320	350	6210

Note. — The critical orbital semimajor axis or the distance at the pericenter of the target stars where the effects of Newtonian attraction equal to the spin-induced ones. Col.[1-4]: $a_\star^{\rm rc}$ (or $a_\star^{\rm zc}$) is the orbital semimajor axis when $\langle\overline{|\delta_{\rm p}\mathbf{R}|}\rangle \simeq \overline{|\delta_{\rm s}\mathbf{R}|}$ (or $\langle\overline{|\delta_{\rm p}Z|}\rangle \simeq \overline{|\delta_{\rm s}Z|}$) for the target star T1 (with $e_\star = 0.88$), in unit of AU. $r_{{\rm per},\star}^{\rm rc} = a_\star^{\rm rc}(1-e_\star)$ [or $r_{{\rm per},\star}^{\rm zc} = a_\star^{\rm zc}(1-e_\star)$] is the corresponding distance of the pericenter, in unit of $r_{\rm g} \sim 0.04$ AU. Col.[5-8]: Similar to Col.[1-4] but for the target star T2 (with $e_\star = 0.3$). For the parameters of these target stars see Table 1.

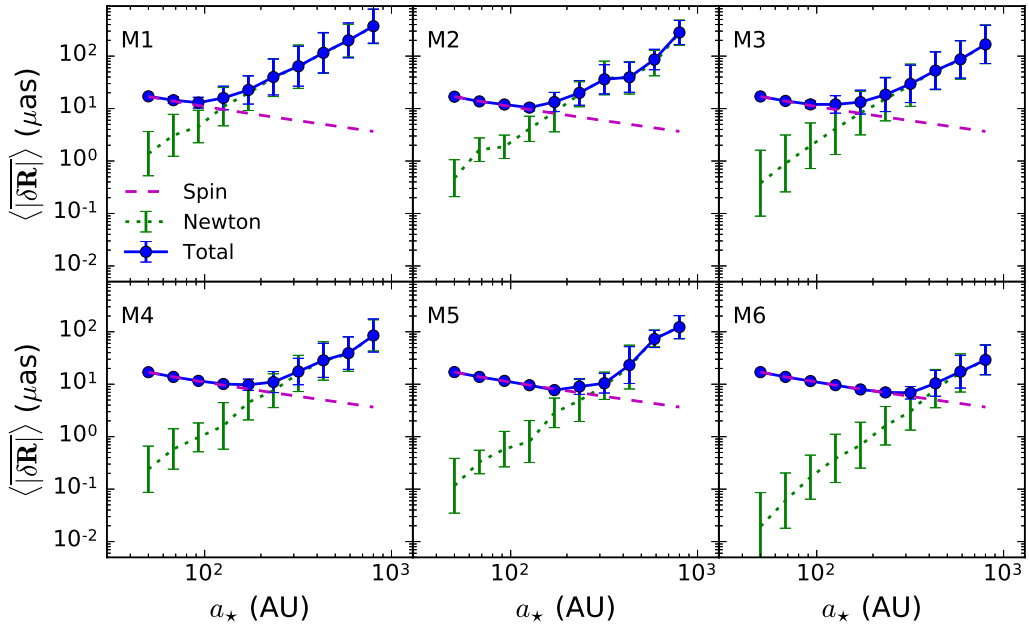

Fig. 9.— Perturbations on the apparent position of target star T1 (see Table 1) as a function of $a_\star$ in different model clusters. $\langle|\overline{\delta_{\rm p}\mathbf{R}}|\rangle$ is defined by Equation 14, i.e., the log-average value of the RMS position displacement in different MC simulations. In each panels, the magenta dashed, green dotted, and the blue solid lines show the spin-induced perturbations, stellar perturbations, and the total perturbations, respectively.

5.1. The model parameters

We adopt six models (M1-M6, see Table 3) with different initial conditions of the star cluster to cope with the large uncertainties in the mass profile within several mpc from the MBH. The details of the model setups are described as follows.

We assume that the cluster consists of perturbers with equal mass $m_{\rm p}$, orbital semimajor axis and eccentricity, i.e., $a_{\rm p}$ and $e_{\rm p}$, following the distribution functions $g(a_{\rm p})$ and $h(e_{\rm p}^2)$, respectively. We assume that the perturbers are with randomly selected initial values of the inclination $I_{\rm p}$, position angle of ascending node $\Omega_{\rm p}$, angle to periapsis $\omega_{\rm p}$ and the time of pericenter passage $t_{0\rm p}$. We assume that the number density of stars in the cluster is given by $n(r) \propto r^{-\gamma}$, and their velocity anisotropy is given by $\beta = 1 - \sigma_{\rm tr}^2/\sigma_{\rm los}^2$, here $\sigma_{\rm tr}$ and $\sigma_{\rm los}$ is the velocity dispersion in the transverse and the line of sight direction, respectively. Then it turns out (Merritt et al. 2010) that $a_{\rm p}$, $e_{\rm p}$ of the perturbers in the cluster follow a distribution $g(a_{\rm p}) \propto a_{\rm p}^{2-\gamma}$, and $h(e_{\rm p}^2) \propto (1-e_{\rm p}^2)^{-\beta}$, $\beta \leq \gamma - 1/2$. Then the total mass and number of perturbers with semimajor axis smaller than $a_{\rm p}$, i.e., $M_{\rm p}(< a_{\rm p})$ and $N_{\rm p}(< a_{\rm p})$, is given by $M_{\rm p}(< a_{\rm p}) = M_1[a_{\rm p}/(1\ {\rm mpc})]^{3-\gamma}$ and $N_{\rm p}(< a_{\rm p}) = M_{\rm p}(< a_{\rm p})/m_{\rm p}$, respectively. Here $M_1 = M_{\rm p}(< 1\ {\rm mpc})$ is the mass of perturbers with $a_{\rm p} < 1$ mpc.

We restrict that 40 AU $< a_{\rm p} <$ 2062 AU (or 0.2 mpc $\lesssim a_{\rm p} \lesssim$ 10 mpc), and denote the total mass and number of perturbers in the cluster by $M_{\rm p}$ and $N_{\rm p}$. The outer boundary (10 mpc) are found large enough for the convergence of the simulation results in this work. The inner boundary (0.2 mpc) is set to avoid perturbers too close to the MBH, which are found slow down the numerical simulation quite significantly and the remove of them cause negligible difference on the simulation results. We avoid those stars of which the periapsis distance is within their tidal radius, i.e., $\simeq (\eta^2 M_\bullet/m_{\rm p})^{1/3}(m_{\rm p}/M_\odot)^{0.47}R_\odot$, where $\eta = 2.21$ (Magorrian & Tremaine 1999). We also avoid the stars with orbital gravitational wave radiation timescale $T_{\rm GW} < 100$Myr, as the total number of these stars may be substantially suppressed due to the rapid orbital decay.

It is still unknown the extent to which the stars and stellar remnants around the vicinity of the MBH are dynamically relaxed by two body interactions. Thus, we consider two extreme cases: (1) They are dynamically relaxed, so that the density profile approaches to the Bahcall-Wolf cusp profile, i.e. $\gamma = 1.75$ (model M1-M4). In this case, it is possible that the stellar mass black holes may dominate the vicinity of the MBH due to the mass segregation effects (e.g., Hopman & Alexander 2006; Alexander & Hopman 2009). We assume that all of the perturbers in the cluster are either low mass main-sequence stars with $m_{\rm p} = 1M_\odot$ or stellar mass black holes with $m_{\rm p} = 10M_\odot$. We set $M_1 = 100M_\odot$ or $30M_\odot$ in each of these cases. Then the total mass of the cluster is given by $M_{\rm p} = 1780M_\odot$ (model M1 and M2) or $530M_\odot$ (model M3 and M4). (2) The mass distribution in the vicinity of the MBH have not yet reached the equilibrium state by two body relaxation; then, the density profile is likely flatter than the BW cusp profiles. We assume that the mass distribution follows a core-like profile with $\gamma = 0.5$ (model M5 and M6). In this case, we assume that the perturbers are all low mass main-sequence stars with $m_{\rm p} = 1M_\odot$ and $M_1 = 5M_\odot$ or $M_1 = 1M_\odot$. Then the total stellar mass is given by $M_{\rm p} = 1581M_\odot$ (model M5) or $316M_\odot$ (model

M6). The total mass and the number of perturbers with orbital semimajor axis smaller than $a_{\rm p}$, i.e., $M_{\rm p}(< a_{\rm p})$ and $N_{\rm p}(< a_{\rm p})$, for all the models in Table 3 are showed in Figure 8.

As we find that the results in this section are insensitive to the eccentricity distribution of the perturber (See also Section 4.2.2), we assume $\beta = 0.5$ for models with $\gamma = 1.75$ and $\beta = -0.5$ for models with $\gamma = 0.5$ in order to fulfill the condition $\beta \leq \gamma - 1/2$.

A target star is assumed embedded in each of these clusters. Similarly to Section 4.2, we consider the target star T1 or T2 (See Table 1). We integrate the perturbations on the target star over three orbits. If without otherwise specified, we assume that the spin parameters are given by $a = 0.99$, $i = 45^\circ$, and $\epsilon = 180^\circ$. For each model in Table 3, $N_{\rm MC}$ independent realizations are performed such that the total number of perturbers in the combined set of integration is ~ 15000. Then we estimate the changes of the orbital elements and the observables of the target star due to the Newtonian and spin-induced perturbations. The details of the results are described in the following sections.

5.2. The perturbed observables of the target star

We denote $\langle\overline{|\delta\mathbf{R}|}\rangle$ and $\langle\overline{\delta Z}\rangle$ as the log-average values of the perturbations of the clusters (Similar to Equation 14), for the position and redshift signals, respectively. The simulation results of $\langle\overline{|\delta\mathbf{R}|}\rangle$ and $\langle\overline{\delta Z}\rangle$ of the target star T1 in clusters M1-M6 are showed in Figure 9 and 10, respectively. We find that similar results can be obtained for the target star T2. Note that both the Newtonian and the spin-induced perturbations felt by the target star T2 are smaller than those by T1, simply due to its smaller eccentricity ($e_\star = 0.3$).

According to Figure 9 and 10, both $\langle\overline{|\delta_{\rm p}\mathbf{R}|}\rangle$ and $\langle\overline{\delta_{\rm p} Z}\rangle$ are increasing functions of $a_\star$, although the slope index of $\langle\overline{|\delta_{\rm p}\mathbf{R}|}\rangle$ is larger than that of $\langle\overline{\delta_{\rm p} Z}\rangle$ as $\langle\overline{|\delta_{\rm p}\mathbf{R}|}\rangle/\langle\overline{\delta_{\rm p} Z}\rangle \propto a_\star^{3/2}$ (See also Section 4.2.2). As the spin-induced effects on both position and redshift are decreasing functions of $a_\star$, i.e., $\overline{|\delta_{\rm s}\mathbf{R}|} \propto a_\star^{-3/2}$ and $\overline{\delta_{\rm s} Z} \propto a_\star^{-2}$, for each model there is a critical orbital semimajor axis of the target star that the effects of Newtonian attraction and the spin equal to each other (See more details in Section 5.4). The combined effects of them (See the blue solid line in each panel of Figure 9 and 10) are thus dominated by the spin-induced effects in the inner region and the Newtonian perturbations in the outer region.

We find that, for a given total mass $M_{\rm p}$, the Newtonian perturbations of a cluster of low mass stars are smaller than that of stellar mass black holes (see also Merritt et al. 2010). For example, the stellar perturbations of the cluster M1 (with $m_{\rm p} = 10M_\odot$ and $N_{\rm p} = 178$) are larger than those of the cluster M2 (with $m_{\rm p} = 1M_\odot$ and $N_{\rm p} = 1780$) by a factor of ~ 2. The reason is probably that M1 consists by more perturbers than M3, such that its potential is more isotropic and the induced stellar perturbations are less significant. Similar results can be obtained if comparing model M3 with M4.

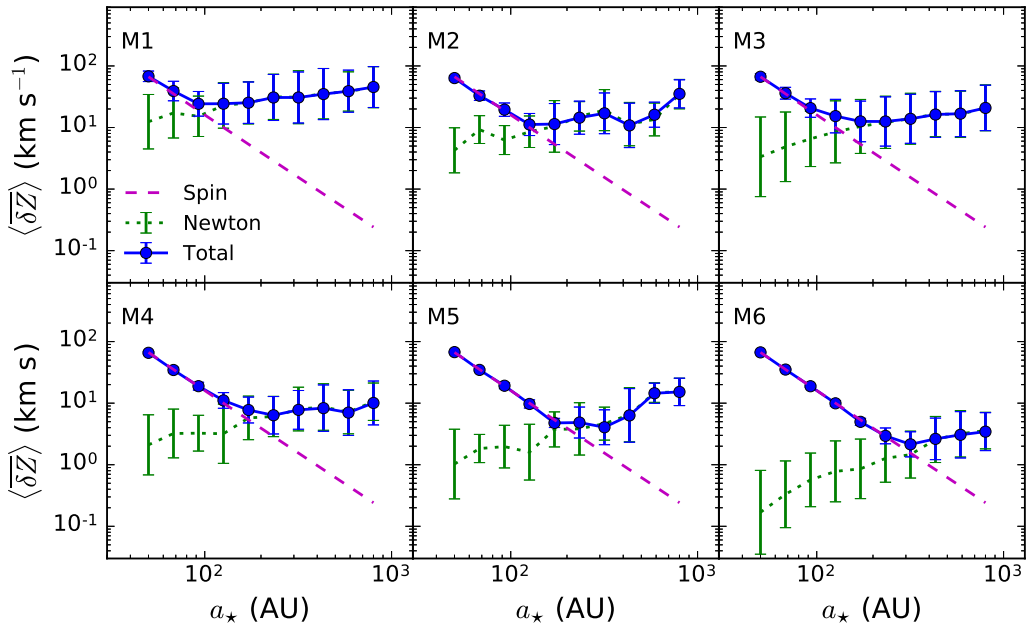

Fig. 10.— Legends similar to those for the Figure 9, but for the perturbations on redshift signal of the target star T1.

Table 5: Stellar Perturbations on the Motion and Signals of the Target Star T1 with $a_\star = 126$ AU.

Name	$\langle\overline{\lvert\delta_{\rm p} f_\star\rvert}\rangle$ [1]	$\langle\overline{\lvert\delta_{\rm p} I_\star\rvert}\rangle$ [2]	$\langle\overline{\lvert\delta_{\rm p}\Omega_\star\rvert}\rangle$ [3]	$\langle\overline{\lvert\delta_{\rm p}\omega_\star\rvert}\rangle$ [4]	$\langle\overline{\lvert\delta_{\rm p}\mathbf{R}\rvert}\rangle$ [5]	$\langle\overline{\lvert\delta_{\rm p} Z\rvert}\rangle$ [6]
M1	14.7	0.23	0.14	0.23	10.9	22.8
M2	5.5	0.08	0.06	0.09	4.1	8.5
M3	5.5	0.1	0.06	0.1	4.1	8.5
M4	2.1	0.04	0.03	0.05	1.6	3.2
M5	1.0	0.03	0.01	0.02	0.8	1.6
M6	0.5	0.01	0.004	0.008	0.4	0.8

Note. — The stellar perturbations on the orbital motion and observables of a target star T1 with $a_\star = 126$ AU. The values for the orbital elements of the target star ($f_\star$, $I_\star$, $\Omega_\star$ and $\omega_\star$) are showed in Col.[1-4] in units of ($'$). The values for the position and redshift signals of the target star are showed in Col.[5] (in units of μas) and Col.[6] (in units of km s^{-1}), respectively. For each values in the table, the standard deviations is $\sim 0.5-1$dex. As a comparison, the RMS spin position and redshift signals of this target star are given by $\overline{|\delta_{\rm s}\mathbf{R}|} = 9.6\mu$as and $\overline{|\delta_{\rm s} Z|} = 10$ km s^{-1}, respectively.

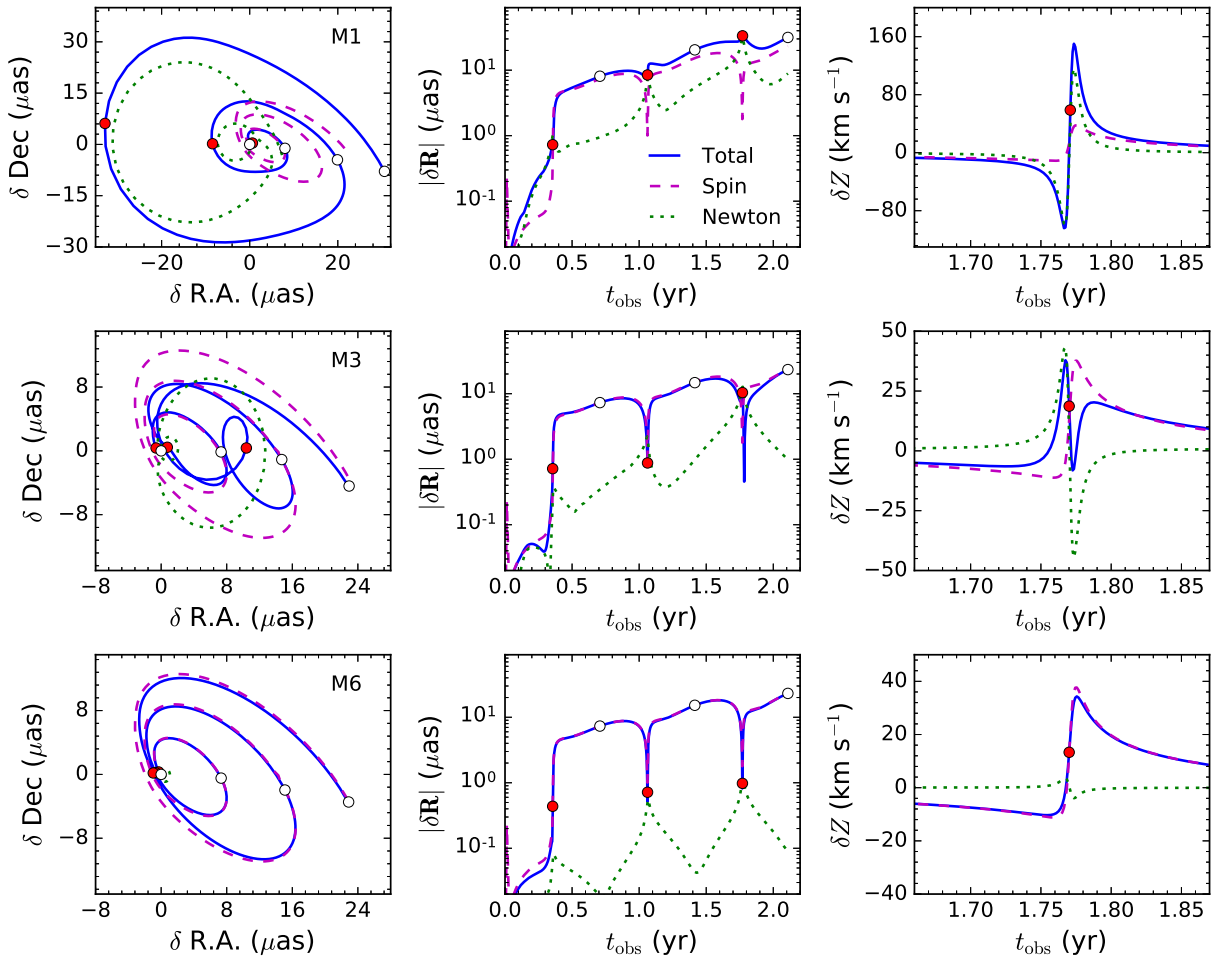

Fig. 11.— Perturbations on the apparent position [$\delta\mathbf{R} = (\delta\text{R.A.}, \delta\text{Dec})$, left panels], its distance ($|\delta\mathbf{R}|$, middle panels) and the redshift (δZ, right panels) of an example target star T1 (see Table 1) with $a_\star = 126$ AU over three orbits (~ 2.2yr). The top, middle and bottom panels show the results when the target star is surrounded by the cluster M1, M3 and M6, respectively. In each panel, the spin-induced perturbations, Newtonian perturbations and the combinations of the above two are showed in the magenta dashed, green dotted, and the blue solid lines, respectively. Red solid and white open circles mark the periapsis and apoapsis passage points of the target star, respectively. Note that the right panels show the difference in the redshift, i.e., δZ, near the third pericenter passage of the target star. The target star is selected out as a typical star from a number of $N_{\rm MC}$ MC runs with $\overline{|\delta_{\rm p}\mathbf{R}|} \sim \langle\overline{|\delta_{\rm p}\mathbf{R}|}\rangle$ and $\overline{\delta_{\rm p}Z} \sim \langle\overline{\delta_{\rm p}Z}\rangle$, here $\langle\overline{|\delta_{\rm p}\mathbf{R}|}\rangle$ and $\langle\overline{\delta_{\rm p}Z}\rangle$ of the target stars are showed in Table 5.

As showed in Section 4, the Newtonian perturbations felt by a target star are mainly attributed to perturbers located around or inside of its orbit ($a_{\rm p} \lesssim a_\star$). For a given total mass $M_{\rm p}$, stellar perturbations of the clusters with cusp profile are larger than those with core profile, because the former contains more perturbers in the inner region than the latter. For example, the mass of cluster M2 is quite similar to that of M5, but the stellar perturbations of the cluster M2 is about $4-5$ times larger than those of the cluster M5 (See Figure 9, 10 and Table 5).

The observables of the target stars with $a_\star \sim 100-400$ AU may be either dominated by Newtonian or spin-induced perturbations, depending on the details of the cluster. Figure 11 shows the perturbations on the observables of a target star T1 with $a_\star = 126$ AU for three models of the cluster (M1, M2 and M3). The target star in each model is selected out from $N_{\rm MC}$ MC runs, with $\overline{|\delta_{\rm p}\mathbf{R}|} \sim \langle\overline{|\delta_{\rm p}\mathbf{R}|}\rangle$ and $\overline{\delta_{\rm p} Z} \sim \langle\overline{\delta_{\rm p} Z}\rangle$ (These values are showed in Table 5). From the top to bottom panels of Figure 11, the dominating factor of the signal gradually changes from stellar to spin-induced perturbations. Figure 11 suggests that for a target star in a cluster: (1) The stellar perturbations on the apparent position and the redshift always peak around the periapsis passage, which are mainly caused by the perturbed orbital period (See Section 4.1.2 and the following Section); (2) The combined perturbations are not similar to either Newtonian or spin-induced ones if they are comparable to each other, i.e., $\overline{|\delta_{\rm p}\mathbf{R}|} \sim \overline{|\delta_{\rm s}\mathbf{R}|}$ or $\overline{\delta_{\rm p} Z} \sim \overline{\delta_{\rm s} Z}$. Thus, a complex morphology of the signal strongly suggests that the contaminations by the stellar perturbations occur. (3) The details of the morphologies/evolutions of the Newtonian perturbations are quite different with respect to the spin-induced effects. According to their distinctive features, in principle, they can be separated from each other.

5.3. The perturbed orbital elements of the target star

We describe the results of the stellar perturbations on the orbital elements in this section. We find that $\langle\overline{\delta_{\rm p}\kappa}\rangle \propto a_\star^\epsilon$, where κ is any orbital elements and ϵ is a slope index depending on the details of the cluster. For models in Table 3, we found $\epsilon \sim 1.9-2.5$ if $\kappa = a_\star$, and $\epsilon \sim 0.7-1.5$ if $\kappa = e_\star$, $I_\star$, $\Omega_\star$, $\omega_\star$ or $f_\star$. The dependence of $\langle\overline{\delta_{\rm p}\kappa}\rangle$ on the parameters of the clusters are quite similar to those of the observables (See Table 5).

Table 5 shows the log-average stellar perturbations on the orbital elements and observables of the target star T1 with $a_\star = 126$ AU. From Table 5, the stellar perturbations cause the precessions of both the argument of periapsis ($\langle\overline{\delta_{\rm p}\omega_\star|}\rangle$) and the orientation of the orbital plane (described by $\langle\overline{\delta_{\rm p} I_\star|}\rangle$ and $\langle\overline{\delta_{\rm p}\Omega_\star|}\rangle$). We found that these results are roughly consistent with the following analytical arguments. The Newtonian precession of the argument of pericenter in each revolution is given by (Madigan et al. 2011)

$$\delta_{\rm p}\omega_\star = 1.72' \times \frac{\mathscr{F}(e_\star,\gamma)}{2-\gamma}\frac{4\times10^6 M_\odot}{M_\bullet} \times \frac{M_{\rm p}(r<a_\star)}{10^3 M_\odot} \tag{15}$$

Here $\mathscr{F}(e_\star, \gamma)$ is a factor depending on the eccentricity of the target star and the density profile. In the case $\gamma = 1.75$, it is given by (Madigan et al. 2011)

$$\mathscr{F}^{-1}(e_\star, 1.75) = 0.681 + \frac{0.975}{\sqrt{1-e_\star}} + 0.373(1-e_\star) \tag{16}$$

$M_{\rm p}(r < a_\star)$ is the enclosed mass within a radii of $r = a_\star$. For a target star with $a_\star = 126$ AU in cluster M1 or M2, $M_{\rm p}(r < 126\ {\rm AU}) \sim 40{\rm M}_\odot$[4]. After three orbits, its RMS Newtonian precession is $\overline{\delta_{\rm p}\omega_\star} \simeq 3 \times \frac{2}{3}\delta_{\rm p}\omega_\star \simeq 0.16'$, which is roughly consistent with the numerical results in model M1 or M2. Note that Equation 15 assume that the potential of the cluster is smooth and isotropic, which may not be fully satisfied in the simulation. The simulated clusters consist by a finite number of perturbers and thus the potential is somewhat anisotropy. This may explain the discrepancies between the results of simulations and that predicted by Equation 15.

The anisotropy of the potential can also lead to effects of the resonant relaxations, which cause the precession of the orbital plane of the target star (e.g., Rauch & Tremaine 1996; Hopman & Alexander 2006). According to Merritt et al. 2010 (its Equation 26 and 27), in each revolution,

$$\frac{|\delta_{\rm p}\mathbf{L}|}{L_c} \simeq \beta_v \frac{m_{\rm p}}{M_\bullet}\sqrt{N_{\rm p}(r < a_\star)} \tag{17}$$

where $\beta_v = 1.8$ and $\frac{|\delta_{\rm p}\mathbf{L}|}{L_c} \simeq (1-e_\star^2)^{1/2}(\delta_{\rm p}I_\star^2 + \sin I_\star^2 \delta_{\rm p}\Omega_\star^2)^{1/2}$ is the relative variation of the angular momentum. After three orbits of the target star, simulations of the cluster M1 (or M2) result in $\frac{|\delta_{\rm p}\mathbf{L}|}{L_c} \simeq 0.11'$ (or $0.04'$). These results are consistent with the predictions of Equation 17, which are $0.1'$ and $0.03'$ for cluster M1 and M2, respectively.

Similar to Section 4.1.2, we found that in most of the performed MC simulations, the Newtonian perturbations on the observables of the target star are mainly caused by the perturbed orbital period, rather than the Newtonian orbital precessions. Take the target star T1 as an example. From Table 5 we can see that $\langle\overline{|\delta_{\rm p}f_\star|}\rangle \gg \langle\overline{|\delta_{\rm p}I_\star|}\rangle$, $\langle\overline{|\delta_{\rm p}\Omega_\star|}\rangle$, or $\langle\overline{|\delta_{\rm p}\omega_\star|}\rangle$. By the rough estimations according to Equation 10 and 11, 12 and 13, it is simple to show that the perturbations on observables due to $\langle\overline{|\delta_{\rm p}f_\star|}\rangle$ are orders of magnitude larger than those due to $\langle\overline{|\delta_{\rm p}I_\star|}\rangle$, $\langle\overline{|\delta_{\rm p}\Omega_\star|}\rangle$ and $\langle\overline{|\delta_{\rm p}\omega_\star|}\rangle$.

5.4. The critical semimajor axis

From Figure 9 and 10, we can see that the total perturbation is dominated by the spin-induced effects in the inner region of the cluster and the stellar perturbations in the outer region. For each model there is a critical orbital semimajor axis of the target star where $\langle\overline{|\delta_{\rm p}\mathbf{R}|}\rangle = \overline{|\delta_{\rm s}\mathbf{R}|}$ or

[4]Note that in cluster M1 or M2, the total mass of perturbers with orbital semimajor axis less than 126 AU is $M_{\rm p}(a_{\rm p} < 126\ {\rm AU}) \sim 54{\rm M}_\odot$. The $M_{\rm p}(r < a_\star)$ is somewhat smaller than $M_{\rm p}(a_{\rm p} < a_\star)$, as at any given moment it is more likely to find perturbers near the apocenter of their eccentric orbits.

$\langle\overline{\delta_{\rm p}Z}\rangle = \overline{\delta_{\rm s}Z}$. Denote $a_\star^{\rm rc}$ or $a_\star^{\rm zc}$ as the critical orbital semimajor axis for the position and redshift signals, respectively, then these values of the target star T1 or T2 and the corresponding pericenter distance ($r_{{\rm per},\star}^{\rm rc} = a_\star^{\rm rc}(1-e_\star)$ and $r_{{\rm per},\star}^{\rm zc} = a_\star^{\rm zc}(1-e_\star)$, respectively) in different models are showed in Table 4. If target stars are with $a_\star$ larger than the critical value, the detection of the spin-induced effects from the observables is likely not feasible as they are quite significantly submerged by the stellar perturbations.

As both the Newtonian and spin-induced perturbations are less significant for target stars with low orbital eccentricities, the resulting critical orbital semimajor axis of the target star T1 is found similar to those of the target star T2. For the clusters explored here, $a_\star^{\rm rc} \simeq 120 - 390$ AU and $a_\star^{\rm zc} \simeq 100 - 330$ AU for the star T1 or $a_\star^{\rm rc} \simeq 100 - 300$ AU and $a_\star^{\rm zc} \simeq 110 - 350$ AU for the star T2. As the different MC realizations lead to about ~ 1 dex scatters on the stellar perturbations, the critical orbital semimajor axis given above may vary up to 25%.

Note that the critical orbital semimajor axis depends also on the spin parameters (its magnitude and orientation). The spin orientation assumed here ($i = 45^\circ$, $\epsilon = 180^\circ$) exhibit modest spin-induced effects. If alternatively choose some other spin magnitude or orientations, then the orbital semimajor axis will be changed accordingly. Take target star T1 as an example. If the spin magnitude of the MBH is smaller, i.e., $a = 0.3$, then for the position signal (or redshift signal), the critical semimajor axis in model M1-M6 are given by $a_\star^{\rm rc} \simeq 100$ AU $- 330$ AU (or $a_\star^{\rm zc} \simeq 60$ AU $- 210$ AU); If we assume $a = 0.99$, $i = 72^\circ$ and $\epsilon = 91^\circ$, such that the spin-induced position displacement is most significant, then $a_\star^{\rm rc} \sim 200$ AU $- 600$ AU; If we assume $a = 0.99$, $i = 38^\circ$ and $\epsilon = 46^\circ$, such that the spin-induced redshift difference is most significant, then $a_\star^{\rm zc} \simeq 110$ AU $- 340$ AU.

6. Discussion

The high order relativistic effects, e.g., frame-dragging and the quadrupole effects, can be used in verifying the theory of general relativity, testing the quasi-Kerr metrics and also the no-hair theory (e.g., Johannsen 2016). However, they should be measured from orbital motion of a target star after a clean removal of the competing perturbations caused by other perturbers. The contaminations of the stellar perturbations cause the deviations of the motion of the target star from the GR predictions. If these contaminating signals are not well removed, they may cause systematic bias of the measured spin parameters or other parameters, e.g., the mass of the black hole and the distance to the GC, obtained by the Markov Chain Monte Carlo fitting scheme. We defer a complete simulation of a data reduction and covariance analysis to future studies.

The complexity of the separation between the stellar perturbation and GR spin effects resides in the fact that the orbits of the perturbers are unknown to the observer. It seems quite challenge to fit the observational data from a number of target stars to recover simultaneously the orbital

parameters of all the surrounding perturbers. In a simple case that the gravitational perturbations can be regarded as a result of a smoothed and static potential, the effects of the stellar perturbations can then be well modeled and removed (Merritt et al. 2010), although it is not clear whether it is a good assumption as the number of stars/ stellar remnants in the very vicinity of the MBH are likely to be small. A wavelet analysis may also help to disentangle the spin effects from the stellar perturbations (Angélil & Saha 2014).

Other dynamical processes can also cause similar shifts in the apparent position and redshift of the target star. For example, gravitational waves and tidal dissipation. These effects are negligible for the S-stars considered in this paper, as they are only important for those S-stars in highly eccentric orbits and/or in extremely tight orbits, e.g., $a_\star \lesssim 10^3 r_{\rm g} \simeq 40$ AU (Psaltis 2012; Psaltis et al. 2013, 2015). It is still possible that there is an IMBH in the GC, with a mass around $10^2 - 10^4 M_\odot$. As the stellar perturbations approximately proportional to the mass of the IMBH (See Figure 3), it can create perturbations on the target star that completely drown the spin effects if its mass is large enough.

Dynamical simulations suggest that pulsars possibly exist in the intermediate vicinity around the MBH in the GC (e.g., Zhang et al. 2014). If they are close enough to the MBH, the high order GR effects, including the frame-dragging and quadrupole effects, can be probed by their precise timing signals. Detections of such pulsars and the measurements of their signal can possibly be realized by the Square Kilometer Array (SKA) (e.g. Pfahl & Loeb 2004; Liu et al. 2012; Psaltis et al. 2016). However, the problems of the stellar perturbations and also the removal of them in the timing signals should also be considered in these studies.

On the other hand, the measurements of the stellar perturbations constrain simultaneously the mass profiles in the vicinity of the MBH in the GC, which is essential for studies of various important dynamical problems in the GC, e.g., the formation and dynamical evolution histories of the S-stars and stellar remnants (e.g. Merritt et al. 2011; Perets et al. 2009; Madigan et al. 2009, 2011; Zhang et al. 2013), the tidal disruptions of the stars by the black holes (e.g. Bromley et al. 2012; Madigan et al. 2011) and the rates of gravitational wave in-spirals (e.g. Merritt et al. 2011; Hopman & Alexander 2006).

7. Conclusion

The S-stars discovered in the close vicinity of the MBH in the GC are anticipated to provide tight constraints on the MBH spin and metric by continuously monitoring their orbits. However, the gravitational attractions of other stars and stellar remnants in this region may deviate the orbit of a target S-star from GR predictions; thus, adequately modeling and removing them is quite essential. To understand comprehensively the stellar perturbations, here we consider both the spin-induced relativistic effects and the Newtonian perturbations felt by the target stars, and their resulting perturbations on the observables of the target star, i.e., the apparent position in the

sky plane and the redshift.

The relativistic numerical methods adopted here rely upon the framework of ZLY15. The gravitational attractions of the background stars/stellar remnants are considered by an additional perturbation term in the Hamiltonian equations of motion of the target star. The apparent orbital motion and the observed redshift of a target star are obtained by the ray-tracing techniques. We find that the simulated variations of the orbital elements of the target star due to the Newtonian perturbations resulting from the method adopted in this work are generally consistent with those from the post-Newtonian method with 2.0 order corrections.

The investigations of the gravitational perturbations by a single perturber can provide helpful hints in understanding the properties and the nature of the stellar perturbations. In this case, the Newtonian perturbations on S2/S0-2 caused by S0-102 are of particular interest. We find that the spin-induced effects on image position (or redshift) can be blurred by the gravitational perturbations from S0-102 alone if the mass of the latter is $\gtrsim 0.6M_\odot$ (or $\gtrsim 0.2M_\odot$), which is very likely as the S-stars are found exclusively B-type stars with masses $\gtrsim 3M_\odot$.

The changes of the observables of the S2/S0-2 result from the changes of its orbital elements. We find that the perturbed observables of S2/S0-2, which is caused by the Newtonian attractions of S0-102, are mainly ascribed to the change of its orbital period. Meanwhile, the Newtonian orbital precessions due to S0-102 induce negligible difference on the observables of S2/S0-2. As a result, the Newtonian perturbations on the observables of S2/S0-2 peak around the time of the pericenter passage in each orbit and evolve quite differently with those of the spin-induced effects. We find that these conclusions also remain true for the general cases that a target star is perturbed by a single or multiple disturbing object(s).

By performing a large number of MC simulations, we study the case of a hypothetical S-star inside the orbits of S2/S0-2 or S0-102 perturbed by a single perturber with various initial conditions. We find that the Newtonian perturbations on the observables of the target star are proportional to the mass of the perturber, and depend complexly on the orbital configurations of both the perturber and the target star. The Newtonian perturbations of a single perturber located inside the orbit of the target star are found to be much more significant than those by a perturber located outside. It is found that in some cases the Newtonian perturbations on the observables due to a single perturber with mass of $10M_\odot$ is large enough to overwhelm the spin-induced effects (See Figure 6 and 7).

So far the mass distribution and its composition in the vicinity of the MBH in the GC are rather uncertain. By performing a large number of numerical simulations that consider a number of possible initial conditions, we investigate the stellar perturbations of a cluster of disturbing objects. We find that, for a given total mass of the cluster, the stellar perturbations due to a cluster of stellar mass black holes (with masses of $10M_\odot$) are larger than those due to a cluster of low mass main-sequence stars (with masses of $1M_\odot$). The stellar perturbations of a cluster with the cusp profile are generally larger than those with the core profile, because it contains more stars

in the inner region. When the central MBH is maximally spinning, the Newtonian perturbation of a cluster can drown the spin-induced signals if the target star is with orbital semimajor axis larger than $100 - 400$ AU.

As showed in the numerical simulations performed in this study, the morphologies of the stellar perturbations seem quite different from the GR spin effects in both the evolutions of the orbital elements and the observables, i.e., the signals of the apparent position and the redshift. Their different features and also the dependences on the model parameters suggest that, in principle, the stellar and the spin-induced perturbations are separable. We defer the separations of these two effects and the accurate measurements of the spin parameters in presence of the Newtonian perturbations to future studies.

We thank Lu Youjun, Yu Qingjuan, and Yang Yi-Jung for helpful suggestions. This work was supported in part by the National Natural Science Foundation of China under grant Nos. 11603083, 11373031, the Fundamental Research Funds for the Central Universities grand No. 161GPY51. This work was also performed in part at the Aspen Center for Physics, which is supported by National Science Foundation grant PHY-1066293. Part of the numerical works were performed in the computing cluster in School of Physics and Astronomy, Sun Yat-Sen University.

REFERENCES

Alexander, T. 1999, ApJ, 527, 835

Angélil, R., Saha, P., & Merritt, D. 2010, ApJ, 720, 1303

Angélil, R., & Saha, P. 2010, ApJ, 711, 157

Angélil, R., & Saha, P. 2011, ApJL, 734, 19

Angélil, R., & Saha, P. 2014, MNRAS, 444, 3780

Alexander, T., & Hopman, C. 2009, ApJ, 697, 1861

Bahcall, J. N., & Wolf, R. A. 1976, ApJ, 209, 214

Bahcall, J. N., & Wolf, R. A. 1977, ApJ, 216, 883

Bartko, H., Martins, F., Trippe, S., Fritz, T. K., Genzel, R., Ott, T., Eisenhauer, F., Gillessen, S., Paumard, T., et al. 2010, ApJ, 708, 834

Boyer, R. H., & Lindquist, R. W. 1967, Journal of Mathematical Physics, 8, 265

Bromley, B. C., Kenyon, S. J., Geller, M. J., & Brown, W. R. 2012, ApJ, 749, L42

Buchholz, R. M., Schödel, R., & Eckart, A. 2009, A&A, 499, 483

Dale, J. E., Davies, M. B., Church, R. P., & Freitag, M. 2009, MNRAS, 393, 1016

Do, T., Ghez, A. M., Morris, M. R., et al. 2009, ApJ, 703, 1323

Do, T., Lu, J. R., Ghez, A. M., et al. 2013a, ApJ, 764, 154

Do, T., Martinez, G. D., Yelda, S., et al. 2013b, ApJ, 779, L6

Fragile, P. C., & Mathews, G. J. 2000, ApJ, 542, 328

Freitag, M., Amaro-Seoane, P., & Kalogera, V. 2006, ApJ, 649, 91

Genzel, R., Eisenhauer, F., & Gillessen, S. 2010, Reviews of Modern Physics, 82, 3121

Ghez, A., Salim, S., Weinberg, N. N., Lu, J. R., Do, T., Dunn, J. K., Matthews, K., Morris, M. R., Yelda, S., Becklin, E. E., et al. 2008, ApJ, 689, 1044

Gillessen, S., Eisenhauer, F., Trippe, S., Alexander, T., Genzel, R., Martins, F., & Ott, T. 2009, ApJ, 692, 1075

Gualandris, A., & Merritt, D. 2009, ApJ, 705, 361

Gualandris, A., Gillessen, S., & Merritt, D. 2010, MNRAS, 409, 1146

Hansen, B. M. S., & Milosavljević, M. 2003, ApJ, 593, L77

Hopman, C., & Alexander, T. 2006, ApJ, 645, L133

Iorio, L. 2011a, MNRAS, 411, 453

Iorio, L. 2011b, Phys. Rev. D, 84, 124001

Iorio, L. 2013, Galaxies, 1, 6

Jaroszynski, M. 1998, Acta Astron., 48, 653

Johannsen, T. 2016, Classical and Quantum Gravity, 33, 113001

Liu, K., Wex, N., Kramer, M., Cordes, J. M., & Lazio, T. J. W. 2012, ApJ, 747, 1

Kerr, R. P. 1963, Physical Review Letters, 11, 237

Kidder, L. E. 1995, Phys. Rev. D, 52, 821

Madigan, A.-M., Levin, Y., & Hopman, C. 2009, ApJ, 697, L44

Madigan, A.-M., Hopman, C., & Levin, Y. 2011, ApJ, 738, 99

Magorrian, J., & Tremaine, S. 1999, MNRAS, 309, 447

Merritt, D., Alexander, T., Mikkola, S., & Will, C. M. 2010, Phys. Rev. D, 81, 062002

Merritt, D., Alexander, T., Mikkola, S., & Will, C. M. 2011, Phys. Rev. D, 84, 044024

Morris, M. 1993, ApJ, 408, 496

Meyer, L., Ghez, A. M., Schödel, R., et al. 2012, Science, 338, 84

Rauch, K., & Tremaine, S. 1996, NewA, 1, 149

Rubilar, G. F., & Eckart, A. 2001, A&A, 374, 95

Paumard, T., Genzel, R., Martins, F., et al. 2006, ApJ, 643, 1011

Perets, H. B., Gualandris, A., Kupi, G., Merritt, D., & Alexander, T. 2009, ApJ, 702, 884

Pfahl, E., & Loeb, A. 2004, ApJ, 615, 253

Preto, M., & Saha, P. 2009, ApJ, 703, 1743

Psaltis, D. 2012, ApJ, 759, 130

Psaltis, D., Li, G., & Loeb, A. 2013, ApJ, 777, 57

Psaltis, D., Wex, N., & Kramer, M. 2015, arXiv:1510.00394

Psaltis, D., Wex, N., & Kramer, M. 2016, ApJ, 818, 121

Sadeghian, L., & Will, C. M. 2011, Classical and Quantum Gravity, 28, 225029

Schödel, R., Merritt, D., & Eckart, A. 2009, A&A, 502, 91

Yu, Q., & Tremaine, S. 2003, ApJ, 599, 1129

Yu, Q., Zhang, F., Lu, Y., 2016, arXiv:1606.07725.

Weinberg, N. N., Milosavljević, M., & Ghez, A. M. 2005, ApJ, 622, 878

Will, C. M. 2008, ApJ, 674, L25

Wisdom, J., & Holman, M. 1991, AJ, 102, 1528

Zhang, F., Lu, Y., & Yu, Q. 2013, ApJ, 768, 153

Zhang, F., Lu, Y., & Yu, Q. 2014, ApJ, 784, 106

Zhang, F., Lu, Y., & Yu, Q. 2015, ApJ, 809, 127

This preprint was prepared with the AAS LaTeX macros v5.2.